Available online at www.sciencedirect.com
SCIENCE DIRECT®
Physics of the Earth and Planetary Interiors 140 (2003) 293–318
PHYSICS OF THE EARTH AND PLANETARY INTERIORS
www.elsevier.com/locate/pepi

Characteristics-based marker-in-cell method with conservative finite-differences schemes for modeling geological flows with strongly variable transport properties

Taras V. Gerya [a,b,*], David A. Yuen [c]

[a] *Institut für Geologie, Mineralogie und Geophysik, Ruhr-Universität Bochum, 44780 Bochum, Germany*
[b] *Russian Academy of Sciences, Institute of Experimental Mineralogy, Chernogolovka, 142432 Moscow, Russia*
[c] *Department of Geology and Geophysics, Minnesota Supercomputing Institute, University of Minnesota, Minneapolis, MN, 55455 USA*

Received 15 December 2002; received in revised form 27 June 2003; accepted 9 October 2003

Abstract

We have designed a 2D thermal–mechanical code, incorporating both a characteristics based marker-in-cell method and conservative finite-difference (FD) schemes. In this paper we will give a detailed description of this code. The temperature equation is advanced in time with the Lagrangian marker techniques based on the method of characteristics and the temperature solution is interpolated back to an Eulerian grid configuration at each timestep. This marker approach allows for the accurate portrayal of very fine thermal structures. For attaining a high relative accuracy in the solution of the matrix equations associated with both the momentum and temperature equations, we have employed the direct matrix inversion technique, which becomes feasible with the advent of very large shared-memory machines. Our conservative finite-difference schemes allow us to capture sharp variations of the stresses and thermal gradients in problems with a strongly variable viscosity and thermal conductivity. We have tested this code with numerous examples drawn from Rayleigh–Taylor instabilities, the descent of a stiff object into a medium with a lower viscosity, viscous heating and flows with non-Netwonian rheology. We have also benchmarked successfully with variable viscosity convection for lateral viscosity contrast up to 10^8. We have delineated the regions in thermal problems where the diffusive nature of the temperature equation changes from its parabolic character locally to a non-linear hyperbolic-like equation due to the presence of variable thermal conductivity. Finally we discuss the applicability of this marker-based and finite-difference technique to other evolutionary equations in geophysics.

Keywords: Mantle convection; Finite-differences; Eulerian/Lagrangian approach; Marker method; Shared-memory

1. Introduction

Today, as modeling of geomechanics is entering a new millennium, geoscientists are faced with more realistic situations in lithospheric and mantle dynamics. These new difficulties arise from the need to model with great fidelity the significant finite deformation in strongly viscous rocks at cold temperatures to contrasting rheological properties across fault zones (Kameyama et al., 1999; Regenauer-Lieb et al., 2001; Kameyama and Kaneda, 2002) and transport properties involving vapor or volatiles (e.g., Woods, 1999; Richard et al., 2002). The rheology of crustal and mantle rocks depends strongly on the temperature, strain-rate, volatile content, grain size and the hydrostatic pressure (e.g., Ranalli, 1995; Karato, 1997).

* Corresponding author. Tel.: +49-234-3223518; fax: +49-234-3214433.
E-mail address: taras.gerya@ruhr-uni-bochum.de (T.V. Gerya).

0031-9201/$ – see front matter © 2003 Elsevier B.V. All rights reserved.
doi:10.1016/j.pepi.2003.09.006

These extenuating physical and dynamical circumstances imposed by the sharply varying viscosity and volatiles indeed represent a major challenge for the momentum equation in geodynamics, unlike those found in the oceanographic or atmospheric sciences. In the limit of creeping flow or the zero Reynolds number regime, the momentum equation becomes a highly non-linear elliptic partial differential equation primarily because of non-linear constitutive relationship between the stress and strain-rate tensors, unlike the other areas in fluid mechanics (e.g., Batchelor, 1967; Balmforth and Provenzale, 2001). The solution of these elliptic partial differential equations has remained a chief computational challenge in solid-earth geophysics (Yuen et al., 2000a,b) because of the ill-conditioned nature of the matrix with vastly varying magnitude in the elements due to the large variations in the rheological properties of rocks. Various types of methods have been devised for solving the elliptic equation for variable viscosity. A popular method has been the multigrid method (Wesseling, 1992; Moresi and Solomatov, 1995). Another non-linearity, not often appreciated up to now in geomechanical-modeling, is that due to variable thermal conductivity in the energy equation. The thermal conductivity of crustal and mantle rocks depends on the temperature and pressure (Hofmeister, 1999) and endows the temperature equation with a strong non-linearity from the square of the ∇T term near the boundary layers (Dubuffet and Yuen, 2000; Dubuffet et al., 2000, 2002) which greatly exacerbates numerical difficulties, produces numerical instabilties and requires more grid points than for constant thermal conductivity situations (Van den Berg et al., 2001). All transport properties of rocks including viscosity, conductivity vary strongly with chemical composition or mineralogy. Similar types of quadractic non-linearity involving the gradient of volatile content, are also found in convection equations with volatile or vapor transport (e.g., Woods, 1999; Richard et al., 2002) Thus, they cause sharp fronts involving multicomponent flows in geological situations, especially when the transport of volatiles is also included in the governing equations in mantle convection (Fountaine et al., 2001; Richard et al., 2002).

From a general geophysical standpoint, we should consider at least three important elements for modeling these kinds of flows:

1. the ability to conserve stresses under conditions involving sharply discontinuous viscosity distribution;
2. the ability to conserve heat and chemical fluxes in the face of sharply varying conductivity, transport coefficient and temperature gradients at the thermal or chemical boundary layers with temperature-dependent conductivity and non-linear transport coefficient, such as in vapor flow at mid-ocean ridges (Fountaine et al., 2001);
3. the ability to conserve scalar quantities with multiscale properties, such as temperature field, chemical species, and density in flows with a strongly advection character, i.e., high Peclet number.

Besides these factors, there are other challenges which are also quite potent, such as phase transitions and its rheological consequences of a dramatic softening from grain-size reduction from nucleation processes in phase transformation (e.g., Riedel and Karato, 1997). We aim to demonstrate in this work that all of these requirements can be achieved by using a marker-in-cell algorithm (e.g., Brackbill and Ruppel, 1986; Brackbill et al., 1988; Brackbill, 1991; Oran and Boris, 1987; Moresi et al., 2003) combining conservative finite-difference (FD) scheme with an arbitrary order in accuracy, an Eulerian/Lagrangian primitive variable formulation based on moving markers which combine both the control volume method (e.g., Patankar, 1980; Albers, 2000) and the accurate trajectories behind the concept of the method of characteristics (Malevsky and Yuen, 1991).

Recent advances in hardware technology with the distributed-shared-memory architecture on supercomputers have prompted us (i) to use large number (10^6–10^8) of markers allowing high-resolution characterization of complex model geometry (e.g., Ten et al., 1999) and (ii) to look again at direct solvers, such as the Gaussian elimination or Cholesky decomposition (Malevsky and Yuen, 1992) for 2D problems because of its prowess in terms of superior relative accuracy over iterative solvers used in many variable viscosity codes (e.g., Moresi and Solomatov, 1995; Tackley, 1996). Recent innovations in the machine architecture on the IBM-SP4, CRAY-1X and the Japanese NEC machines have put at least 16 Gbytes of shared memory available on a single node. Within the next 2 years the next generation of these machines

will offer 64–128 Gbytes on a single node. It is therefore our challenge to prepare for the onslaught of these ultra-lage distributed-shared-memory architecture. The anticipation of these coming technological innovations has figured prominently in our computational strategy laid out in this paper.

In Section 2 we will provide in some details the implementation of these algorithms on conservative finite-difference schemes for modeling flows with variable viscosity and conductivity. We then move to a description of the marker scheme combined with this conservative finite-difference method and the novel treatment of the temperature equation by this hybrid scheme combining the best of the Lagrangian and Eulerian approaches. We then demonstrate in Section 3 by some benchmarks the efficacy of our hybrid method and present the results on various types of flows characterized by variable viscosity, viscous heating and variable thermal conductivity. The final section will be our discussion and conclusions.

2. Basic background of the numerical modeling scheme

2.1. Principal equations

In this section we will describe in detail the numerical implementation of the fundamental conservation equations of mass, momentum and energy and the constitutive relationships between stress and strain-rate needed for modeling geomechanical problems in the two-dimensional creeping flow regime. They will be applicable in convective heat-transfer problems involving multiphase viscous fluids in the presence of a gravitational body force term. This set of partial differential equations comprises, first of all, the Stokes equations of slow flow where the inertial terms are dropped. Eqs. (1) and (2) are the second-order elliptic equations in the velocity field (v).

$$\frac{\partial \sigma_{xx}}{\partial_x} + \frac{\partial \sigma_{xz}}{\partial z} = \frac{\partial P}{\partial x} - \rho(T, C) g_x, \tag{1}$$

$$\frac{\partial \sigma_{zz}}{\partial z} + \frac{\partial \sigma_{xz}}{\partial x} = \frac{\partial P}{\partial z} - \rho(T, C) g_z. \tag{2}$$

$$\sigma_{xx} = 2\eta\varepsilon_{xx}$$

$$\sigma_{xz} = 2\eta\varepsilon_{xz}$$

$$\sigma_{zz} = 2\eta\varepsilon_{zz}$$

$$\varepsilon_{xx} = \frac{\partial v_x}{x}$$

$$\varepsilon_{xz} = \frac{1}{2}\left(\frac{\partial v_x}{\partial z} + \frac{\partial v_z}{\partial x}\right)$$

$$\varepsilon_{zz} = \frac{\partial v_z}{\partial z}$$

This is followed by the constitutive relationship between the stress (σ) and strain-rate (ε), where the transport coefficient η represents the viscosity, which depends on the temperature (T), pressure (P), chemical components (C) and strain-rate.

The conservation of mass is given by the continuity equation in which we keep density to be a constant in all terms except for the buoyancy force, where both temperature and volatile content come into play. This level of truncation is known as the Boussinesq approximation on which most mantle convection codes were built on (e.g., Moresi and Solomatov, 1995; Trompert and Hansen, 1996; Albers, 2000)

$$\frac{\partial v_x}{\partial x} + \frac{\partial v_z}{\partial z} = 0. \tag{3}$$

As part of our new computational strategy, instead of using the Eulerian frame of reference, we have elected to go to the Lagrangian frame of reference for temperature equation, and the extended Boussinesq approximation (Christensen and Yuen, 1985) has been used to take into account adiabatic and viscous heating contributions. These two terms are deemed significant in many important tectonic situations, such as mountain-belt collision (Kincaid and Silver, 1996). The temperature equation (Eq. (4)) is a second-order in space and first-order in time and it is non-linear in T because of the variable thermal conductivity.

$$\rho C_p \left(\frac{DT}{Dt}\right) = \frac{\partial q_x}{\partial x} + \frac{\partial q_z}{\partial z} + H_r + H_a + H_s, \tag{4}$$

$$q_x = k(T, P) \times \left(\frac{\partial T}{\partial x}\right),$$

$$q_z = k(T, P) \times \left(\frac{\partial T}{\partial z}\right),$$

$$H_r = \text{const},$$

$$H_a = T\alpha\left[v_x\left(\frac{\partial P}{\partial x}\right) + v_z\left(\frac{\partial P}{\partial z}\right)\right] \approx T\alpha\rho[v_x g_x + v_z g_z],$$

$$H_s = \sigma_{xx}\varepsilon_{xx} + \sigma_{zz}\varepsilon_{zz} + 2\sigma_{xz}\varepsilon_{xz},$$

where DT/Dt represents the substantive time derivative and we have used markers here to follow the temporal development of both the temperature field and the chemical components field, as they are being advected by the common velocity field. Other notations in Eqs. (1)–(4) are: x and z denotes, respectively, the horizontal and vertical coordinates, in m, v_x and v_z are components of the velocity vector in $m\,s^{-1}$; t time in s; σ_{xx}, σ_{xz}, σ_{zz} are components of the viscous deviatoric stress tensor in units of Pa; ε_{xx}, ε_{xz}, ε_{zz} are components of the strain-rate tensor in s^{-1}; P the pressure in Pa; T the temperature in K; q_x and q_z are horizontal and vertical heat fluxes in $W\,m^{-2}$; η the effective viscosity in Pa s, depending on pressure, temperature and strain-rate (e.g., Ranalli, 1995); ρ the density in $kg\,m^{-3}$, depending on chemical composition, phase assemblage (e.g., presence of dense minerals, melt, e.g., Gerya et al., 2001, 2002), pressure and temperature; g_x and g_z denote components of the vector of acceleration within the gravity field for the x–z 2D coordinate system, $m\,s^{-2}$; $k(T, P)$ is the variable thermal conductivity coefficient in $W\,m^{-1}\,K^{-1}$, depending on the temperature and pressure; C_p the isobaric heat capacity in $J\,kg^{-1}\,K^{-1}$; H_r, H_a, and H_s denote, respectively, radioactive, adiabatic and shear heating production in $W\,m^{-3}$ (for simplicity of calculation of H_a slight deviations of dynamic pressure gradients $\partial P/\partial x$ and $\partial P/\partial z$ from ρg_x and ρg_z values are neglected).

2.2. Computational strategy with markers

In order to achieve the goals set out in geo-modeling as outlined in the introduction, we have designed a conservative finite-difference scheme over an irregularly-spaced staggered grid in an Eulerian grid configuration (Fig. 1). The irregularly spaced grid is extremely useful in handling geodynamical situations with multiple-scale character, such as in a subducting slab and the wedge flow above it (e.g., Davies and Stevenson, 1992). This Eulerian FD method is then combined with the moving marker technique

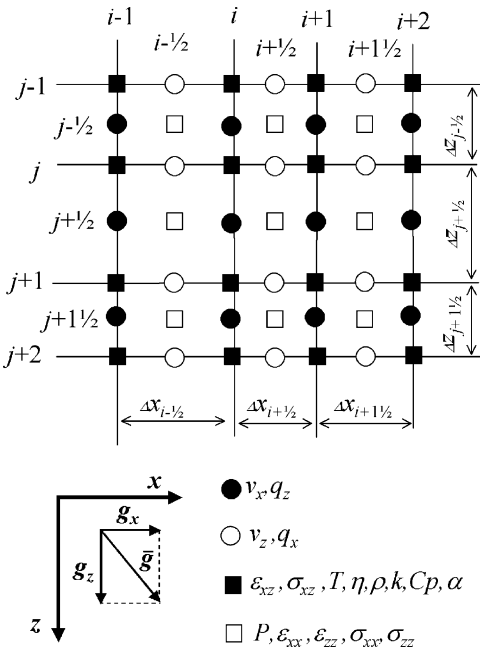

Fig. 1. Schematic representation of non-regular rectangular staggered Eulerian grid used for numerical solution of Eq. (1)–(4). g_x and g_z are components of gravitational acceleration in the x–z coordinate frame. Different symbols correspond to the nodal points for different scalar properties, vectors and tensors. i, $i+1/2$, etc. and j, $j+1/2$, etc. indexes represent the staggered grid and denote, respectively, the horizontal and vertical positions of four different types of nodal points. Many variables (v_x, v_z, σ_{xx}, σ_{xz}, σ_{zz}, ε_{xx}, ε_{xz}, ε_{zz}, P, T, η, ρ, k, C_p, etc.), up to around 25 at grid point, are part of the voluminous output in this code.

or the Lagrangian approach, shown in Fig. 2, to solve Eqs. (1)–(4). We show in Fig. 3 a schematic flow-chart for updating at each timestep the evolutionary equations contained in (1)–(4). We have solved Eqs. (1)–(4) based on a combination of finite control volume method (e.g., Patankar, 1980; Albers, 2000), combined with an arbitrary order of accuracy in the finite-difference discretization (Fornberg, 1995) and method of characteristics (e.g., Malevsky and Yuen, 1991; De Smet et al., 2000) implemented via the moving marker technique (e.g., Hockney and Eastwood, 1981; Christensen and Yuen, 1984; Weinberg and Schmeling, 1992; Schott and Schmeling, 1998; Gerya et al., 2000). The steps are as follows (detailed explanation of these steps is given in Sections 2.3–2.5):

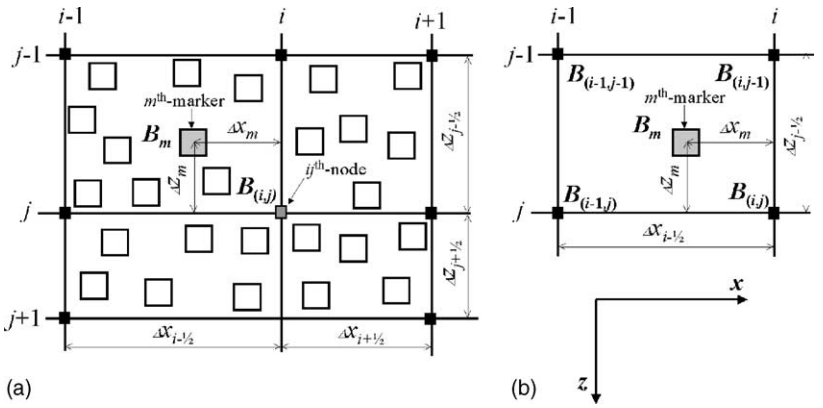

Fig. 2. Schematic representation of geometrical relations used for the adopted first-order of accuracy interpolation schemes of a parameter B (a) from the markers to Eulerian nodes and (b) from Eulerian nodes back to markers. Each marker holds information concerning the temperature T, position coordinates, three components of the strain tensor, representing the deformation history and the chemical components C.

1. Solving 2D Eqs. (1)–(3) by directly inverting the global matrix with a Gaussian elimination method, which is chosen because of its programming simplicity, stability and high accuracy.
2. Calculating the non-linear shear- and adiabatic heating terms $H_{s(i,j)}$ and $H_{a(i,j)}$ at the Eulerian nodes.
3. Calculating $(DT/Dt)_{(i,j)}$ values at the Eulerian nodes by an explicit scheme.
4. Defining an optimal time step Δt for temperature equation. We use a minimum time step value satisfying the following conditions: given absolute time step limit on the order of a minimal characteristic timescale for the modelled processes; given relative marker displacement step limit (typically 0.1–0.2 of minimal grid step) corresponding to calculated velocity field (see Step 1); given absolute nodal temperature change limit (typically 1–20 K) corresponding to calculated explicit $(DT/Dt)_{(i,j)}$ values (see Step 3).
5. Solving the non-linear temperature equation implicitly by a direct Gaussian inversion method.
6. Interpolating calculated nodal temperature changes (see Step 6 at Fig. 3) from the Eulerian nodes to the markers and calculating new marker temperatures $({}^{t}T_m)$.
7. Using a fourth-order in space/first-order in time explicit Runge–Kutta scheme for advecting all markers throughout the mesh according to the globally calculated velocity field v (see Step 1).
8. Calculating globally the scalar physical properties (η_m, ρ_m, C_m, C_{pm}, k_m, C, etc.) from the markers.
9. Interpolating temperature and other scalar properties, such as C, C_p, from the markers to Eulerian nodes. Returning to Step 1 at the next timestep.

We have implemented the above computational algorithm in a new computer code, called I2VIS, which is written in the C—computer language in order to facilitate post-processing. This code has been developed on the basis of our previous thermo-mechanical code based on finite-differences, (I2), which employed finite-difference method over a half-staggered grid and used the marker technique (Gerya et al., 2000).

2.3. Interpolation of scalar fields, vectors and tensors

According to our algorithmic approach the temperature field and other scalar properties (η, ρ, C_p, C, k, etc.) are represented by scalar values ascribed for the multitudinous markers initially distributed on a fine regular marker mesh with a small ($\leq$1/2 of marker grid distance) random displacement (Fig. 2). The effective values of all these parameters at the Eulerian nodal points are interpolated from the markers at each time step. An average number of markers per grid cell commonly vary from $n \times (10^0$–$10^2)$ depending on the complexity of model geometry (e.g., Brackbill, 1991; Ten et al., 1999; Gerya et al., 2003). The following standard first-order of accuracy scheme (e.g.,

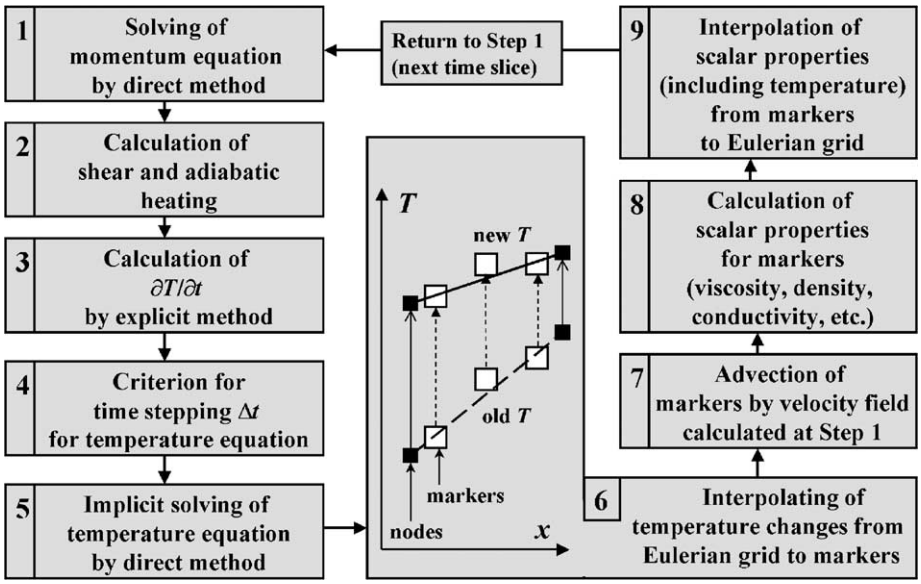

Fig. 3. Flow chart representing the adopted computational strategy used in the programming of the computer code I2VIS. Panel for Step 6 shows the scheme for interpolating the calculated temperature changes from the Eulerian grid to the moving markers.

Fornberg, 1995) is used to calculate an interpolated value of a parameter $B_{(i,j)}$ for *ij*th-node using values (B_m) ascribed to all markers found in the four surrounding cells (Fig. 2a)

$$B_{(i,j)} = \frac{\sum_m B_m w_{m(i,j)}}{\sum_m w_{m(i,j)}}, \quad (5)$$

$$w_{m(i,j)} = \left[1 - \frac{\Delta x_m}{\Delta x_{(i-1/2)}}\right] \times \frac{1 - \Delta z_m/\Delta z_{(j-1/2)}}{\Delta x_{(i-1/2)} \times \Delta z_{(j-1/2)}},$$

where $w_{m(i,j)}$ represents a statistical weight of *m*th-marker at the *ij*th-node; $\Delta x_m/\Delta x_{(i-1/2)}$ and $\Delta z_m/\Delta z_{(i-1/2)}$ are normalized distances from *m*th-marker to *ij*th-node. In the case of non-uniform Eulerian grid, we use a two-dimensional bisectioning method to determine the corresponding grid cell in which the marker is located (Fig. 2a). For interpolating the nodes along the margins we use only the markers found inside an Eulerian grid independent of the boundary conditions. The slight inaccuracy of interpolation for marginal nodes is compensated by our increasing the grid resolution at the boundaries. The use of a higher-order accurate interpolation schemes produces undesirable numerical fluctuations in scalar, vector and tensor properties interpolated in the proximity of sharp transitions. For example, negative values of viscosity are calculated at the fixed Eulerian nodes at thermal boundary layers with sharp (>10^3) viscosity contrast, by using a second-order FD scheme (e.g., Fornberg, 1995).

For the same reason we have used a standard first-order of accuracy (e.g., Fornberg, 1995) procedure for the reversed problem of interpolating the scalar properties (including calculated temperature changes), vectors and tensors from the corresponding Eulerian nodal points (see different types of Eulerian nodes in Fig. 1) back to the markers and other geometrical points (e.g., other nodes). The values of a parameter *B* defined in four Eulerian nodes surrounding a given marker (Fig. 2b) are used for calculating an effective value of the parameter *B* for *m*th-marker as follows:

$$\begin{aligned} B_m = {} & \left[1 - \frac{\Delta x_m}{\Delta x_{(i-1/2)}}\right] \times \left[1 - \frac{\Delta z_m}{\Delta z_{(j-1/2)}}\right] \times B_{(i,j)} \\ & + \left[\frac{\Delta x_m}{\Delta x_{(i-1/2)}}\right] \times \left[1 - \frac{\Delta z_m}{\Delta z_{(j-1/2)}}\right] \times B_{(i-1,j)} \\ & + \left[1 - \frac{\Delta x_m}{\Delta x_{(i-1/2)}}\right] \times \left[\frac{\Delta z_m}{\Delta z_{(j-1/2)}}\right] \times B_{(i,j-1)} \\ & + \left[\frac{\Delta x_m}{\Delta x_{(i-1/2)}}\right] \times \left[\frac{\Delta z_m}{\Delta z_{(j-1/2)}}\right] \\ & \times B_{(i-1,j-1)}, \end{aligned} \quad (6)$$

where B_m denote the value of parameter B for mth-marker. Scheme (6) is used uniformly, when we interpolate the velocity, stresses, strain-rates, pressure, temperature and other properties from nodal points to markers. Since our staggered grid represents, in fact, the superposition of four simple rectanugular grids corresponding to different scalar fields, vectors and tensor (see four different symbols for gridpoints in Fig. 1), these Eulearian grids are used individually for interpolating the respective field variables.

The standard first-order interpolation schemes yield equally good results in cases (1)–(4) comparing to more complex, higher-order (e.g., Fornberg, 1995) interpolation schemes.

2.4. Finite-difference schemes for discretizing the momentum and continuity equations

Apart of the stability and superior accuracy by comparison to the non- and half-staggered grids staggered grid shown in Fig. 1 is ideally suitable for the discretization of the momentum and continuity equations (e.g., Fornberg, 1995). We used a standard formal procedure (e.g., Patankar, 1980; Oran and Boris, 1987; Fornberg, 1995; Albers, 2000) for the formulation of FD scheme representing momentum Eqs. (1) and (2) in a conservative form: (i) momentum equation is formulated in term of derivatives of stress components, (ii) these derivatives are discretized by using first-order accurate schemes, (iii) different stress components are ascribed to the specific $\sigma_{xx}/\sigma_{zz}/P$- and σ_{xz}-nodes of the grid (see, respectively, open and solid squares in Fig. 1) located between pairs of v_x- and v_z-nodes of the grid (see, respectively, solid and open circles in Fig. 1) and (iv) identical formulations of stress components are used in discretizing momentum Eq. (1) and (2) in v_x- and v_z-nodes. The following FD scheme is a discretized form for representing Eqs. (1)–(3) to a first-order accuracy in the control volume representation (e.g., Patankar, 1980; Albers, 2000), which allows for the conservation of the viscous stresses between the v_x- and v_z-nodes (see Fig. 1 for the indexing of the grid points):

$$\left[\frac{\partial\sigma_{xx}}{\partial x}\right]_{(i,j+1/2)}+\left[\frac{\partial\sigma_{xz}}{\partial z}\right]_{(i,j+1/2)}-\left[\frac{\partial P}{\partial x}\right]_{(i,j+1/2)}=-\frac{1}{2}[\rho_{(i,j)}+\rho_{(i,j+1)}]\times g_{x(i,j+1/2)} \quad (7)$$

$$\left[\frac{\partial\sigma_{xx}}{\partial x}\right]_{(i,j+1/2)}=\frac{2[\sigma_{xx(i+1/2,j+1/2)}-\sigma_{xx(i-1/2,j+1/2)}]}{\Delta x_{(i-1/2)}+\Delta x_{(i+1/2)}},$$

$$\left[\frac{\partial\sigma_{xz}}{\partial z}\right]_{(i,j+1/2)}=\frac{\sigma_{xz(i,j+1)}-\sigma_{xz(i,j)}}{\Delta z_{(j+1/2)}},$$

$$\left[\frac{\partial P}{\partial x}\right]_{(i,j+1/2)}=\frac{2[P_{(i+1/2,j+1/2)}-P_{(i-1/2,j+1/2)}]}{\Delta x_{(i-1/2)}+\Delta x_{(i+1/2)}},$$

where i, $i+1/2$ and j, $j+1/2$ indexes denote, respectively, the horizontal and vertical positions of nodal points corresponding to the different physical parameters (Fig. 1) within the staggered grid (Wesseling, 1992).

$$\left[\frac{\partial\sigma_{zz}}{\partial z}\right]_{(i+1/2,j)}+\left[\frac{\partial\sigma_{xz}}{\partial x}\right]_{(i+1/2,j)}-\left[\frac{\partial P}{\partial z}\right]_{(i+1/2,j)}=-\frac{1}{2}[\rho_{(i,j)}+\rho_{(i+1,j)}]\times g_{z(i+1/2,j)}, \quad (8)$$

$$\left[\frac{\partial\sigma_{zz}}{\partial z}\right]_{(i+1/2,j)}=\frac{2[\sigma_{zz(i+1/2,j+1/2)}-\sigma_{zz(i+1/2,j-1/2)}]}{\Delta z_{(j-1/2)}+\Delta z_{(j+1/2)}},$$

$$\left[\frac{\partial\sigma_{xz}}{\partial x}\right]_{(i+1/2,j)}=\frac{\sigma_{xz(i+1,j)}-\sigma_{xz(i,j)}}{\Delta x_{(i+1/2)}},$$

$$\left[\frac{\partial P}{\partial z}\right]_{(i+1/2,j)}=\frac{2[P_{(i+1/2,j+1/2)}-P_{(i+1/2,j-1/2)}]}{\Delta z_{(j-1/2)}+\Delta z_{(i+1/2)}},$$

and

$$\left[\frac{\partial v_x}{\partial x}\right]_{(i-1/2,j-1/2)}+\left[\frac{\partial v_z}{\partial z}\right]_{(i-1/2,j-1/2)}=0; \quad (9)$$

where

$$\sigma_{xx(i-1/2,j+1/2)}=\tfrac{1}{2}[\eta_{(i-1,j)}+\eta_{(i-1,j+1)}+\eta_{(i,j)}+\eta_{(i,j+1)}]\times\varepsilon_{xx(i-1/2,j+1/2)}$$

$$\sigma_{xx(i+1/2,j+1/2)}=\tfrac{1}{2}[\eta_{(i,j)}+\eta_{(i,j+1)}+\eta_{(i+1,j)}+\eta_{(i+1,j+1)}]\times\varepsilon_{xx(i+1/2,j+1/2)}$$

$$\sigma_{xz(i,j)} = 2\eta_{(i,j)}\varepsilon_{xz(i,j)},$$

$$\sigma_{xz(i,j+1)} = 2\eta_{(i,j+1)}\varepsilon_{xz(i,j+1)},$$

$$\sigma_{xz(i+1,j)} = 2\eta_{(i+1,j)}\varepsilon_{xz(i+1,j)},$$

$$\sigma_{zz(i+1/2,j-1/2)} = \tfrac{1}{2}[\eta_{(i,j-1)} + \eta_{(i,j)} + \eta_{(i+1,j-1)} + \eta_{(i+1,j)}] \times \varepsilon_{zz(i+1/2,j-1/2)}$$

$$\sigma_{zz(i+1/2,j+1/2)} = \tfrac{1}{2}[\eta_{(i,j)} + \eta_{(i,j+1)} + \eta_{(i+1,j)} + \eta_{(i+1,j+1)}] \times \varepsilon_{zz(i+1/2,j+1/2)}$$

$$\varepsilon_{xx(i-1/2,j+1/2)} = \left[\frac{\partial v_x}{\partial x}\right]_{(i-1/2,j+1/2)}$$

$$\varepsilon_{xx(i+1/2,j+1/2)} = \left[\frac{\partial v_x}{\partial x}\right]_{(i+1/2,j+1/2)}$$

$$\varepsilon_{xz(i,j)} = \frac{1}{2}\left[\frac{\partial v_x}{\partial z} + \frac{\partial v_z}{\partial x}\right]_{(i,j)},$$

$$\varepsilon_{xz(i,j+1)} = \frac{1}{2}\left[\frac{\partial v_x}{\partial z} + \frac{\partial v_z}{\partial x}\right]_{(i,j+1)},$$

$$\varepsilon_{xz(i+1,j)} = \frac{1}{2}\left[\frac{\partial v_x}{\partial z} + \frac{\partial v_z}{\partial x}\right]_{(i+1,j)},$$

$$\varepsilon_{zz(i+1/2,j-1/2)} = \left[\frac{\partial v_z}{\partial z}\right]_{(i+1/2,j-1/2)}$$

$$\varepsilon_{zz(i+1/2,j+1/2)} = \left[\frac{\partial v_z}{\partial z}\right]_{(i+1/2,j+1/2)}$$

In the FD formulation of Eqs. (7) and (8) the stress is decomposed into a product of the viscosity and the strain-rate. The latter is formulated, using an arbitrary order accurate FD scheme (Fornberg, 1995) for the derivatives of velocity. This formulation is also used in finite difference treatment of seismic wave propagation (Virieux, 1986). First-order accurate FD scheme for these derivatives most suitable for problems with sharply varying viscosity are written as

$$\left[\frac{\partial v_x}{\partial x}\right]_{(i-1/2,j-1/2)} = \frac{v_{x(i,j-1/2)} - v_{x(i-1,j-1/2)}}{\Delta x_{(i-1/2)}},$$

$$\left[\frac{\partial v_x}{\partial x}\right]_{(i-1/2,j+1/2)} = \frac{v_{x(i,j+1/2)} - v_{x(i-1,j+1/2)}}{\Delta x_{(i-1/2)}},$$

$$\left[\frac{\partial v_x}{\partial x}\right]_{(i+1/2,j+1/2)} = \frac{v_{x(i+1,j+1/2)} - v_{x(i,j+1/2)}}{\Delta x_{(i+1/2)}},$$

$$\left[\frac{\partial v_x}{\partial z}\right]_{(i,j)} = \frac{2[v_{x(i,j+1/2)} - v_{x(i,j-1/2)}]}{\Delta z_{(j-1/2)} + \Delta z_{(j+1/2)}},$$

$$\left[\frac{\partial v_x}{\partial z}\right]_{(i,j+1)} = \frac{2[v_{x(i,j+3/2)} - v_{x(i,j+1/2)}]}{\Delta z_{(j+1/2)} + \Delta z_{(j+3/2)}},$$

$$\left[\frac{\partial v_x}{\partial z}\right]_{(i+1,j)} = \frac{2[v_{x(i+1,j+1/2)} - v_{x(i+1,j-1/2)}]}{\Delta z_{(j-1/2)} + \Delta z_{(j+1/2)}},$$

$$\left[\frac{\partial v_z}{\partial x}\right]_{(i,j)} = \frac{2[v_{z(i+1/2,j)} - v_{z(i-1/2,j)}]}{\Delta x_{(i-1/2)} + \Delta x_{(i+1/2)}},$$

$$\left[\frac{\partial v_z}{\partial x}\right]_{(i,j+1)} = \frac{2[v_{z(i+1/2,j+1)} - v_{z(i-1/2,j+1)}]}{\Delta x_{(i-1/2)} + \Delta x_{(i+1/2)}},$$

$$\left[\frac{\partial v_z}{\partial x}\right]_{(i+1,j)} = \frac{2[v_{z(i+3/2,j)} - v_{z(i+1/2,j)}]}{\Delta x_{(i+1/2)} + \Delta x_{(i+3/2)}},$$

$$\left[\frac{\partial v_z}{\partial z}\right]_{(i-1/2,j-1/2)} = \frac{v_{z(i-1/2,j)} - v_{z(i-1/2,j-1)}}{\Delta z_{(j-1/2)}},$$

$$\left[\frac{\partial v_z}{\partial z}\right]_{(i+1/2,j-1/2)} = \frac{v_{z(i+1/2,j)} - v_{z(i+1/2,j-1)}}{\Delta z_{(j-1/2)}},$$

$$\left[\frac{\partial v_z}{\partial z}\right]_{(i+1/2,j+1/2)} = \frac{v_{z(i+1/2,j+1)} - v_{z(i+1/2,j)}}{\Delta z_{(j+1/2)}},$$

We invert for the global matrix by a highly accurate, direct (Gaussian) method for the simultaneous solution of momentum Eqs. (7) and (8), and continuity Eq. (9) also combined with linear equations describing the boundary conditions for the velocity. We would like to emphasize that continuity Eq. (9) with the velocity vectors as the variables is solved directly to machine accuracy with the direct matrix inversion method, thus obviating the usual need of using the streamfunction formulation or other means of incompressibility. In what follows, the momentum Eqs. (7) and (8) are solved for $v_{x(i,j+1/2)}$ and $v_{z(i+1/2,j)}$, respectively, while the continuity Eq. (9) is solved for $P_{(i-1/2,j-1/2)}$. Incompressible continuity Eq. (9) does not initially contain $P_{(i-1/2,j-1/2)}$ and the solution is guaranteed by the order of processing

during the inversion of the global matrix (see Fig. 1 for indexing): Eq. (9) for pressure in a given cell (e.g., $P_{(i-1/2,j-1/2)}$, see Fig. 1), is processed after Eqs. (7) and (8) for all surrounding v_x- and v_z-nodes (e.g., $v_{x(i-1,j-1/2)}$, $v_{x(i,j-1/2)}$, $v_{z(i-1/2,j-1)}$ and $v_{z(i-1/2,j)}$, see Fig. 1). Accordingly, the overall numbering of $P_{(i-1/2,j-1/2)}$, $v_{x(i,j+1/2)}$ and $v_{z(i+1/2,j)}$ for the global matrix defining the order of processing of respective equations is done as follows:

$$M_{\text{matrix}} = 3(i \times N_{\text{lines}} + j) \quad \text{for } P_{(i-1/2,j-1/2)},$$

$$M_{\text{matrix}} = 3(i \times N_{\text{lines}} + j) + 1 \quad \text{for } v_{x(i,j+1/2)},$$

$$M_{\text{matrix}} = 3(i \times N_{\text{lines}} + j) + 2 \quad \text{for } v_{z(i+1/2,j)},$$

where M_{matrix} is the parameter index in the global matrix and N_{lines} is the total number of horizontal lines for the grid (see Fig. 1 for the positions of these lines).

The relative accuracy of solving the momentum and continuity equations commonly vary from 10^{-15} to 10^{-13} depending on the viscosity variations. However, in several cases lower (10^{-6}) accuracy has been obtained, as a result of strong sharp variations in the viscosity (e.g., for some models with $\geq 10^6$ viscosity contrast for the adjacent nodes).

2.5. Numerical techniques for solving temperature equation

Malevsky and Yuen (1991) developed a characteristics-based method for solving the temperature equation to avoid the numerical oscillations from advection at the high Rayleigh number regime. This method, however, requires an increasing amount of operations for tracing characteristics back to an initial temperature distribution in the case of strongly chaotic advection pattern. To avoid this problem, we have implemented a characteristics based marker technique commonly used for advection of material field properties, such as the density, viscosity, chemical composition etc. (e.g., Hockney and Eastwood, 1981; Weinberg and Schmeling, 1992; Schott and Schmeling, 1998; De Smet et al., 2000; Gerya et al., 2000). According to this approach the temperature field is represented by temperature values (T_m) assigned for the multitudinous markers initially distributed on a fine marker mesh (see Section 2.3). The effective temperature $T_{(i,j)}$ field at the Eulerian nodes is then interpolated from the markers at each time step, using relation (5). The effective temperatures at the boundary nodes are then replaced by values satisfying the thermal boundary conditions.

We used a standard formal procedure (e.g., Patankar, 1980; Oran and Boris, 1987; Fornberg, 1995; Albers, 2000) for the formulation of FD scheme representing temperature Eq. (4) in a conservative form: (i) temperature equation is formulated in term of derivatives of heat fluxes, (ii) these derivatives are discretized by using first-order accurate schemes, (iii) different heat fluxes are ascribed to the specific q_x- and q_z-nodes of the grid (see, respectively, open and solid circles in Fig. 1) located between the pairs of T-nodes of the grid (see solid squares in Fig. 1) and (iv) identical formulations of heat fluxes are used in discretizing temperature Eq. (4) in T-nodes. The calculation of the temporal changes in the temperature at the Eulerian nodes is based on the following implicit first-order FD scheme representing Eq. (4) in a conservative (e.g., Oran and Boris, 1987) form, which allows for the conservation of the heat fluxes between the T nodal points (see Fig. 1 for the indexing of the grid points):

$$\rho_{(i,j)} C_{\text{p}(i,j)} \left[\frac{DT}{Dt}\right]_{(i,j)} - \left[\frac{\partial q_x}{\partial x}\right]_{(i,j)} - \left[\frac{\partial q_z}{\partial z}\right]_{(i,j)} = H_{\text{r}(i,j)} + H_{\text{a}(i,j)} + H_{\text{s}(i,j)}, \tag{10}$$

$$\left[\frac{DT}{Dt}\right]_{(i,j)} = \frac{{}^1T_{(i,j)} - T_{(i,j)}}{\Delta t},$$

$$\left[\frac{\partial q_x}{\partial x}\right]_{(i,j)} = \frac{2[{}^1q_{x(i+1/2,j)} - {}^1q_{x(i-1/2,j)}]}{\Delta x_{(i-1/2)} + \Delta x_{(i+1/2)}},$$

$$\left[\frac{\partial q_z}{\partial z}\right]_{(i,j)} = \frac{2[{}^1q_{z(i,j+1/2)} - {}^1q_{x(i,j-1/2)}]}{\Delta z_{(j-1/2)} + \Delta z_{(j+1/2)}},$$

$${}^1q_{x(i-1/2,j)} = \frac{1}{2}[k_{(i-1,j)} + k_{(i,j)}] \times \left[\frac{\partial({}^1T)}{\partial x}\right]_{(i-1/2,j)};$$

$${}^1q_{x(i+1/2,j)} = \frac{1}{2}[k_{(i,j)} + k_{(i+1,j)}] \times \left[\frac{\partial({}^1T)}{\partial x}\right]_{(i+1/2,j)};$$

$${}^1q_{z(i,j-1/2)} = \frac{1}{2}[k_{(i,j-1)} + k_{(i,j)}] \times \left[\frac{\partial({}^1T)}{\partial z}\right]_{(i,j-1/2)};$$

$${}^1q_{z(i,j+1/2)} = \frac{1}{2}[k_{(i,j)} + k_{(i,j+1)}] \times \left[\frac{\partial({}^1T)}{\partial z}\right]_{(i,j+1/2)};$$

$$H_{a(i,j)} = T_{(i,j)}\alpha_{(i,j)}\rho_{(i,j)}[v_{x(i,j)}g_{x(i,j)} + v_{z(i,j)}g_{z(i,j)}];$$

$$H_{s(i,j)} = \sigma_{xx(i,j)}\varepsilon_{xx(i,j)} + \sigma_{zz(i,j)}\varepsilon_{zz(i,j)} + 2\sigma_{xz(i,j)}\varepsilon_{xz(i,j)};$$

where indexes 1 denote values for the next time instant to be reached by the time-stepping and Δt is the optimal time step (see above, in Section 2.2); $H_{r(i,j)}$, $H_{a(i,j)}$, $H_{s(i,j)}$, $\alpha_{(i,j)}$, $\rho_{(i,j)}$, $C_{p(i,j)}$, $\sigma_{xx(i,j)}$, $\varepsilon_{xx(i,j)}$, $\sigma_{zz(i,j)}$, $\varepsilon_{zz(i,j)}$, $\sigma_{xz(i,j)}$, $\varepsilon_{xz(i,j)}$, $v_{x(i,j)}$, and $v_{z(i,j)}$ are values of the corresponding parameters for the ij-node: scalar properties are interpolated from the markers using relation (5), vectors and tensors are also interpolated from the corresponding surrounding nodes from Eq. (6). In the FD formulation of Eq. (10) the heat fluxes are decomposed into a product of the thermal conductivity and the temperature gradients. These quantities are formulated by using an arbitrary order accurate method FD (Fornberg, 1995) for the derivatives of the temperature. First-order accurate FD schemes for these derivatives most suitable for problems with strongly varying thermal conductivity are

$$\left[\frac{\partial(^1T)}{\partial x}\right]_{(i-1/2,j)} = \frac{^1T_{(i,j)} - {}^1T_{(i-1,j)}}{\Delta x_{(i-1/2)}};$$

$$\left[\frac{\partial(^1T)}{\partial x}\right]_{(i+1/2,j)} = \frac{^1T_{(i+1,j)} - {}^1T_{(i,j)}}{\Delta x_{(i+1/2)}}$$

$$\left[\frac{\partial(^1T)}{\partial z}\right]_{(i,j-1/2)} = \frac{^1T_{(i,j)} - {}^1T_{(i,j-1)}}{\Delta z_{(j-1/2)}};$$

$$\left[\frac{\partial(^1T)}{\partial z}\right]_{(i,j+1/2)} = \frac{^1T_{(i,j+1)} - {}^1T_{(i,j)}}{\Delta z_{(j+1/2)}}.$$

In the absence of strong heat sources $H_{r(i,j)}$, $H_{a(i,j)}$ and $H_{s(i,j)}$ implicit scheme of Eq. (10) is unconditionally stable (e.g., Oran and Boris, 1987). If strong heat sources are present timestep Δt is optimized using standard (e.g., Oran and Boris, 1987) criteria (see Step 4 in Section 2.2).

For solving the temperature equations with non-linearities present we invert directly by a global matrix with a high accuracy direct (Gaussian) method. The matrix also contains the linear equations associated with the thermal boundary conditions. The overall numbering of $^1T_{(i,j)}$ for the global matrix defining the order of processing of respective equations is done as follows:

$$M_{matrix} = i \times N_{lines} + j,$$

where M_{matrix} is the parameter index in the global matrix and N_{lines} the total number of horizontal lines for the grid (see Fig. 1 for the positions of these lines). The relative accuracy of the inverted solution spans between 10^{-15} and 10^{-13}.

The changes in the effective temperature field for the Eulerian nodes are calculated as

$$\Delta T_{(i,j)} = {}^1T_{(i,j)} - T_{(i,j)}. \quad (11)$$

Correspondent temperature increments for markers ΔT_m are then interpolated from the nodes using relation (6) in order to calculate new marker temperatures ^tT_m as

$$^tT_m = T_m + \Delta T_m. \quad (11a)$$

The interpolation of the calculated temperature changes from the Eulerian nodal points to the moving markers prevents effectively the problem of numerical diffusion. This feature represents one of the highlights of our computation strategy for solving the temperature equation using markers. This method does not produce any smoothing of the temperature distribution between adjacent markers (Fig. 3, diagram for Step 6), thus resolving the thermal structure of a numerical model in much finer details.

However, the main problems with treating advection diffusion methods using this incremental update scheme is that all manner of stirred-structures and instabilities on a subgrid (marker) scale cannot be damped out by grid-scale corrections. For example, in case of strong chaotic mixing of markers, our method may produce numerical oscillations of thermal field ascribed to the adjacent markers. These oscillations do not damp out with time on a characteristic heat diffusion timescale. The introduction of a consistent sub-grid diffusion operation, which does not change the convergence of the grid scale diffusion solution is the way around this. We use here a weak numerical diffusion occurring over a characteristic heat diffusion timescale. This is implemented by correcting the marker temperatures ^tT_m according to the relation

$$ {}^{t}T_{m(D)} = {}^{1}T_{m} - [{}^{1}T_{m} - {}^{t}T_{m}] \times \exp\left(\frac{-d\,\Delta t}{\Delta t_0}\right), \tag{12} $$

$$ \Delta t_0 = \frac{C_{pm}\rho_m}{\{k_m[2/(\Delta x_{(i-1/2)})^2 + 2/(\Delta z_{(j-1/2)})^2]\}}, $$

where Δt_0 is a characteristic timescale of the local heat diffusion defined for the corresponding cell of the grid (Fig. 2b); ${}^{t}T_{m(D)}$ the mth-marker temperature corrected for the numerical diffusion; d the dimensionless numerical diffusion coefficient (we use empirical values in the range of $0 \leq d \leq 1$); ${}^{1}T_m$, C_{pm}, ρ_m and k_m are interpolated, respectively, from ${}^{1}T_{(i,j)}$, $C_{p(i,j)}$, $\rho_{(i,j)}$ and $k_{(i,j)}$ values for nodes using the relation (6). Eq. (12) require decay of a difference between ${}^{1}T_m$ and ${}^{t}T_m$ values within the time comparable with the characteristic timescale (Δt_0) of local heat diffusion.

Compensating temperature corrections $\Delta T_{(i,j)A}$ are first calculated at the Eulerian nodes according to relation (5) as

$$ \Delta T_{(i,j)A} = \frac{\sum_m ({}^{t}T_{m(D)} - {}^{t}T_m) w_{m(i,j)}}{\sum_m w_{m(i,j)}}. \tag{13} $$

These nodal corrections values are then used for compensating correction of temperatures for markers by using relation (6) as follows:

$$ {}^{t}T_{m(D-A)} = {}^{t}T_{m(D)} - \Delta T_{m(A)}. \tag{13a} $$

where ${}^{t}T_{m(D-A)}$ is the final corrected mth-marker temperature; $\Delta T_{m(A)}$ is compensating temperature correction interpolated for mth-marker from $\Delta T_{(i,j)A}$ values for Eulerian nodes using relation (6).

Introducing the numerical diffusion operation removes unrealistic subgrid oscillations (see Section 3.8) over the characteristic local heat diffusion timescale without affecting the accuracy of numerical solution of the temperature equation (see Sections 3.4 and 3.6). Realistic subgrid oscillations will, however, be preserved by this scheme been related for example to the rapid mixing by advection dominating flows.

3. Verification of the numerical schemes by calibrating various cases

In this section we will display results taken from carrying out several calibrating tests of the numerical solutions in order to verify the efficacy of our methods for a variety of circumstances relevant to geothermo-mechanics. These will include

(a) sharply discontinuous viscosity distribution (test 1 and 2);
(b) strain-rate dependent viscosity (test 3);
(c) non-steady development of temperature field (test 4);
(d) shear heating for temperature dependent viscosity (test 5);
(e) advection of a sharp temperature front (test 6);
(f) heat conduction for temperature-dependent thermal conductivity (test 7);
(g) thermal convection with a large viscosity contrast in the temperature-dependent viscosity and for both constant and temperature-dependent thermal conductivity (tests 8 and 9).

Numerical experiments discussed in Sections 3.1–3.9 show stability and high accuracy of the algorithm at low to moderate resolution for both Eulerian nodes ($n \times (10^2$–$10^3)$) and markers ($n \times (10^3$–$10^4)$). These experiments require small computation time of several minutes (Sections 3.1–3.7) to several tens of minutes (Sections 3.8–3.9) on ordinary PC. The method allows for the high resolution of $n \times (10^4$–$10^5)$ Eulerian nodes and $n \times (10^6$–$10^7)$ markers for various types of 2D numerical experiments (e.g., Gerya et al., 2004) requiring computation time varying from several hours to several days on single processor depending on the type of the computer used.

3.1. Rayleigh–Taylor instabilities involving a two-layer cross-section and gravity

A series of tests have been carried out for a two-layer model with a non-slip condition on the top and at the bottom and symmetry conditions along the vertical walls. An initial sinusoidal disturbance of the boundary between the upper (η_1, ρ_1) and the lower (η_2, ρ_2) layer of thickness h has a small amplitude (y) and a wave length (λ). This produces favorable conditions for studying the velocity of the diapiric growth (v_z) given by the relation (Ramberg, 1981)

$$ K = \frac{2v_z\eta_2}{y(\rho_1 - \rho_2)hg}, \tag{14} $$

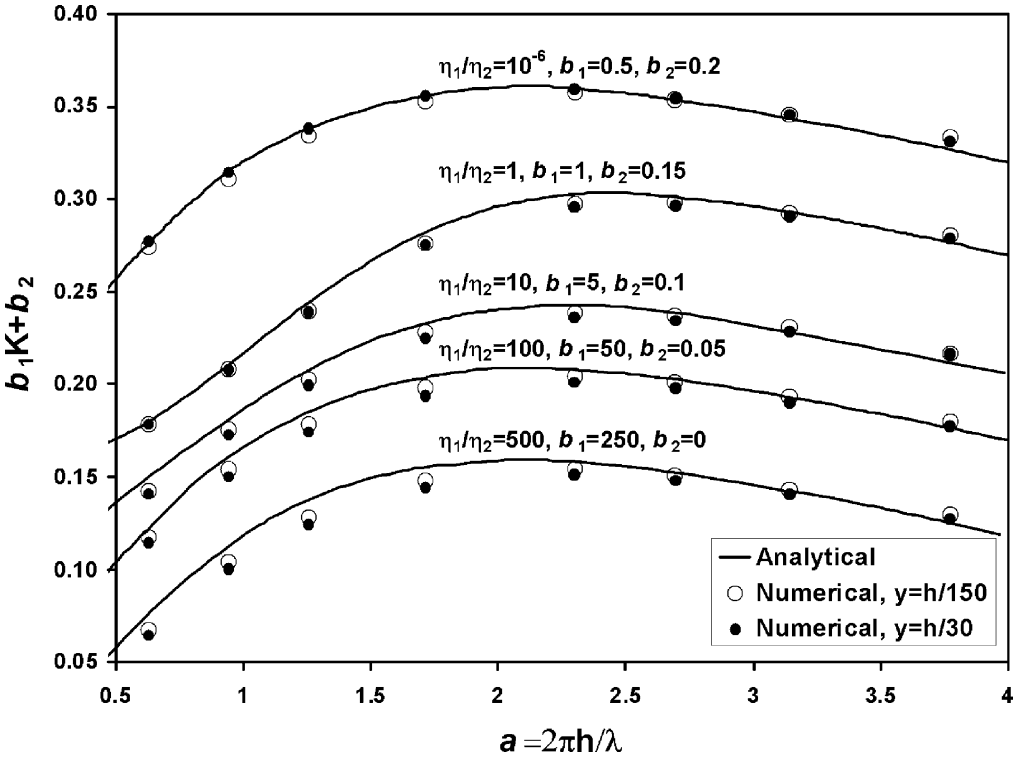

Fig. 4. Numerical solutions for the case of the Rayleigh–Taylor instability of a two-layer cross-section in the gravity field. Numerical and analytical solutions are compared for the factor of growth K at different viscosity contrast between the upper (η_1) and the lower (η_2) layer and different wave number ($a = 2\pi h/\lambda$, where h is the layer thickness, and λ the wavelength) and amplitude (y) of initial sinusoidal disturbance at the layer boundary. Grid resolution of the model: 32×31 nodes, 23,250 markers.

where K is a dimensionless factor of growth. Fig. 4 compares both the numerical and analytical solutions for the factor of growth of the diapir estimated at different values of y, λ and η_1/η_2. Good accuracy of $\pm$2–5% is determined at large variations of the disturbance wave length and the layers viscosity contrasts ($\eta_1/\eta_2 = 10^{-6}$ to 5×10^2). This result shows the correct numerical solutions of Eqs. (1)–(3) in the case of sharp changes in density and viscosity across a boundary layer.

3.2. Sinking of a hard rectangular block into a medium with a lower viscosity

The results of this test are displayed in Fig. 5. According to our physical intuitions, the deformation of the block vanish with increasing viscosity contrast and dynamics of sinking at high viscosity contrast does not depend on the absolute value of the viscosity of the block. This test proves the accurate conservation properties of our numerical procedure in terms of preserving the geometry at large deformation and high (10^2–10^6) viscosity contrast between the harder block and the softer surroundings.

3.3. Channel flow with non-Newtonian rheology

This test is conducted to check the numerical solution of Eqs. (1)–(3) for flows with a strong strain-rate dependent rheology, which is characterisic of dislocation creep (Ranalli, 1995). The computation is carried out for vertical flow of a viscous non-Newtonian (with a power-law index $n = 3$) medium in a channel of the width L in the absence of gravity. Boundary conditions are taken as follows: given vertical pressure gradient, $\partial P/\partial z$, along the channel and non-slip conditions at

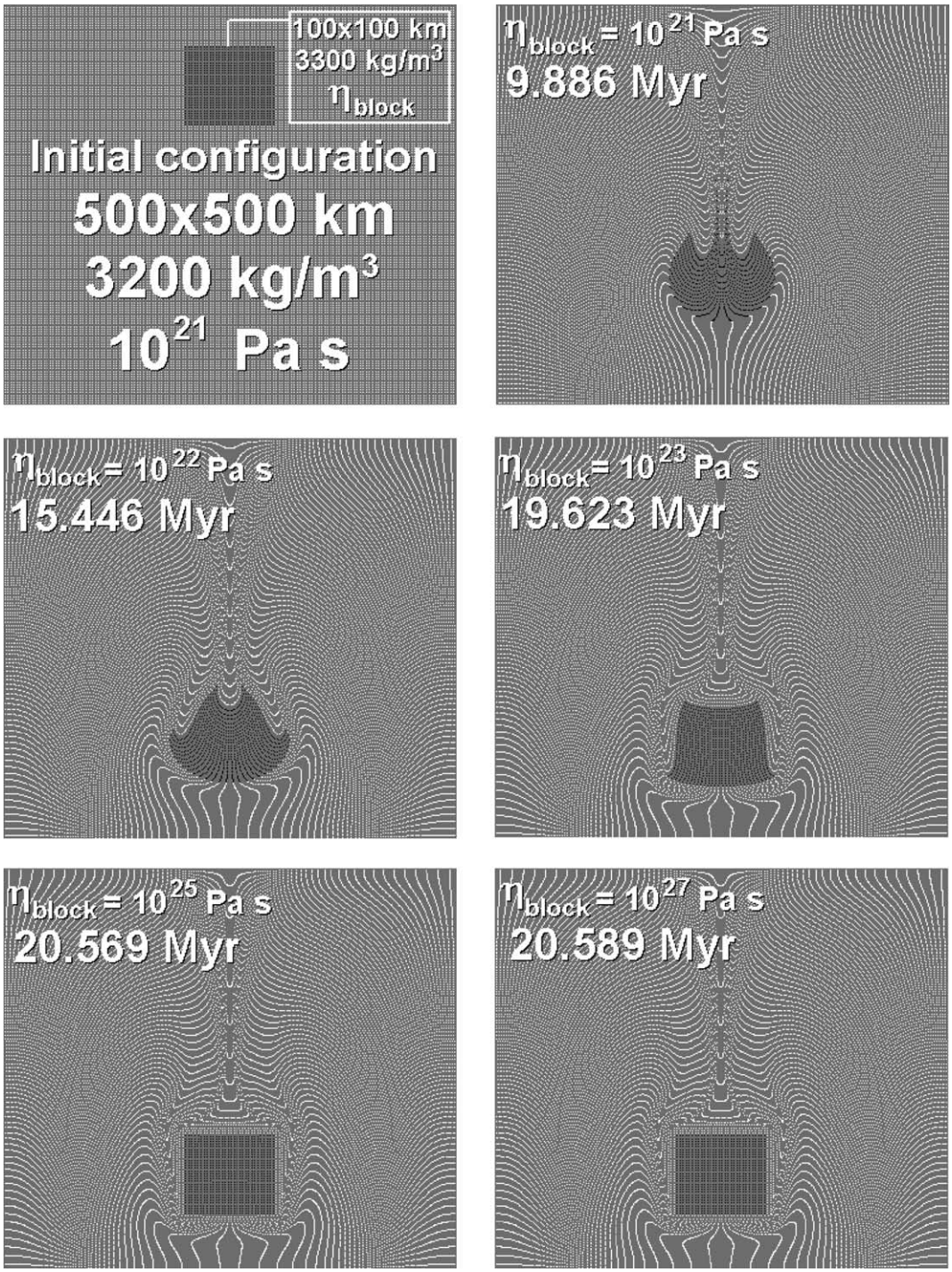

Fig. 5. Results of numerical experiments for the sinking of rectangular block at different viscosity contrast between the block and the surrounding soft medium (see text for discussion). Boundary conditions: free slip at all boundaries. Black and white dots represent positions of markers for the block and the medium, respectively. Grid resolution of the model is 51×51 nodes, 22,500 markers.

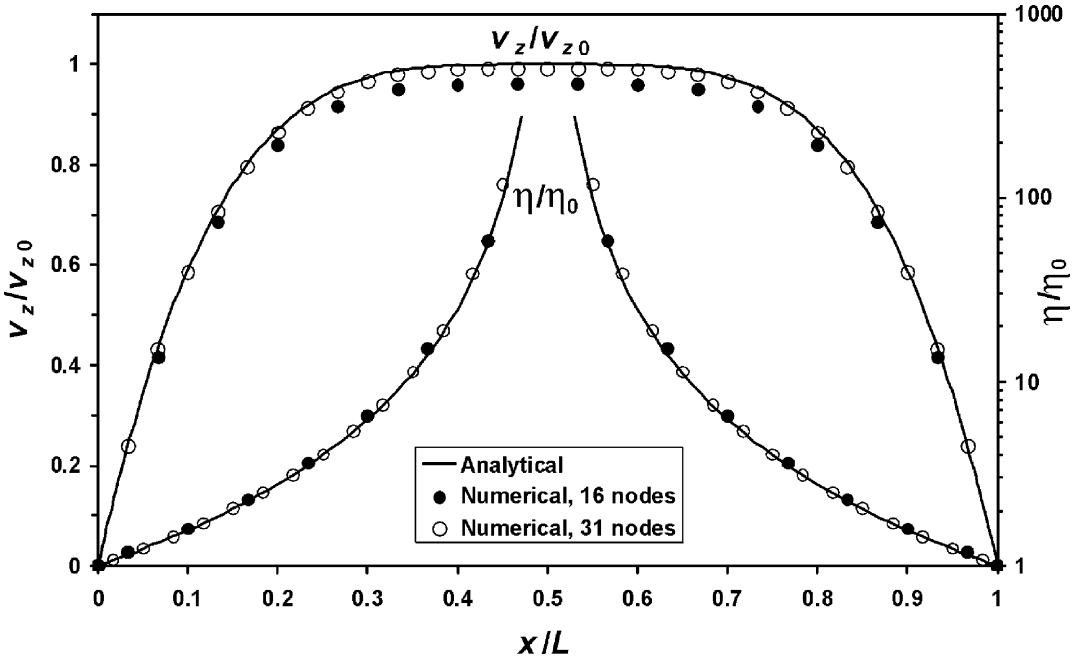

Fig. 6. The results of test of numerical solution for the case of power-law flow in the channel of width L. v_{z0} is the velocity in the center of the channel, η_0 the viscosity at the walls (see Eq. (17)). Different symbols show the numerical results for the different lateral resolution of the model (31 nodes/150 markers and 16 nodes/75 markers).

the walls. The viscosity of the non-Newtonian flow is defined by the following rheological equation

$$\sigma_{xz} = M(\partial v_z/\partial x)^{1/3}, \tag{15}$$

where M is rheological constant in Pa s$^{1/3}$. The analytical solution for the horizontal profile of vertical velocity v_z and effective strain-rate dependent viscosity $\eta = \sigma_{xz}/(\partial v_z/\partial x)$ across the channel is derived from Eqs. (2) and (15) as follows:

$$v_z = v_{z0}\left[1 - \left(\frac{2x}{L} - 1\right)^4\right], \tag{16}$$

$$\eta = \frac{\eta_0}{(2x/L - 1)^2}, \tag{17}$$

$$v_{z0} = -L^4\frac{[(\partial P/\partial z)/M]^3}{64},$$

$$\eta_0 = \frac{4M^3}{[(\partial P/\partial z)L]^2},$$

where v_{z0} is the velocity in the center of the channel, η_0 the viscosity at the walls. Fig. 6 compares the numerical and analytical solutions for the horizontal distribution of velocity and viscosity across the channel. We can see clearly that the numerical and analytical solutions accord quite well, suggesting that our numerical procedure can solve correctly the momentum equation in the case of strain-rate dependent non-linear rheology with $n = 3$.

3.4. Non-steady temperature distribution in a Newtonian channel flow

This time-dependent test is performed to ascertain the numerical accuracy of the temperature Eq. (4) in the temporal development (heat advection coupled with heat diffusion). The calculations are carried out by using a model of the vertical flow of a heat-conductive medium of constant viscosity in a channel in the absence of gravity. Boundary conditions are taken as follows: given vertical pressure gradient, $\partial P/\partial z$, along the channel, non-slip conditions and

$T = \text{const}$ and $\partial T/\partial z = \text{const}$ at the walls. The initial conditions are $T = T_0$ and $\partial T/\partial x = 0$. The horizontal steady-state profile for vertical velocities, v_z, is defined by the equation

$$v_z = \frac{4v_z^0(Lx - x^2)}{L^2}, \qquad (18)$$

$$v_{z0} = \frac{-L^2(\partial P/\partial z)}{8\eta},$$

where L is the width of the channel; η the viscosity of the channel; v_{z0} the vertical velocity in the center of the channel. The corresponding temperature changes in the channel as a function of time are given by the following series expansion (Tikhonov and Samarsky, 1972; Gerya et al., 2000)

$$\Delta T(x, t) = \sum_{m=1}^{\infty} F_m E_{mt} \sin\left[\frac{\pi(2m-1)x}{L}\right], \qquad (19)$$

where

$$F_m = \frac{-8\xi L^2}{[\pi(2m-1)]^3},$$

$$E_{mt} = \frac{L^2}{[\pi(2m-1)]^2} \frac{\{1 - \exp(-[\pi(2m-1)/L]^2\kappa t)\}}{\kappa},$$

$$\kappa = \frac{k}{\rho C_p},$$

$$\xi = \frac{4v_{z0}(\partial T_0/\partial z)}{L^2},$$

where $\Delta T(x, t)$ is the temperature in the channel as a function of the spatial coordinates and time; κ the constant thermal diffusivity in $m^2\,s^{-1}$. When calculating analytical solution an infinite summation of Eq. (19) is cut after $m = 20$ due to negligible contribution of members of higher-order. Eq. (19) does not account for shear heating: in this numerical test it is considered as negligible. Fig. 7 shows that numerical and analytical results agree very well for calculations performed both with ($d = 1$) and without ($d = 0$) numerical diffusion included (see Eq. (12)).

3.5. Couette flow with viscous heating

These tests are conducted to verify the numerical solution of the coupled momentum and temperature equations for flows with temperature dependent rheology in the situation of strong shear heating for a moderate lateral grid resolution (32 nodes, 310 markers across). We have considered numerically the computation for a vertical Couette flow in the absence

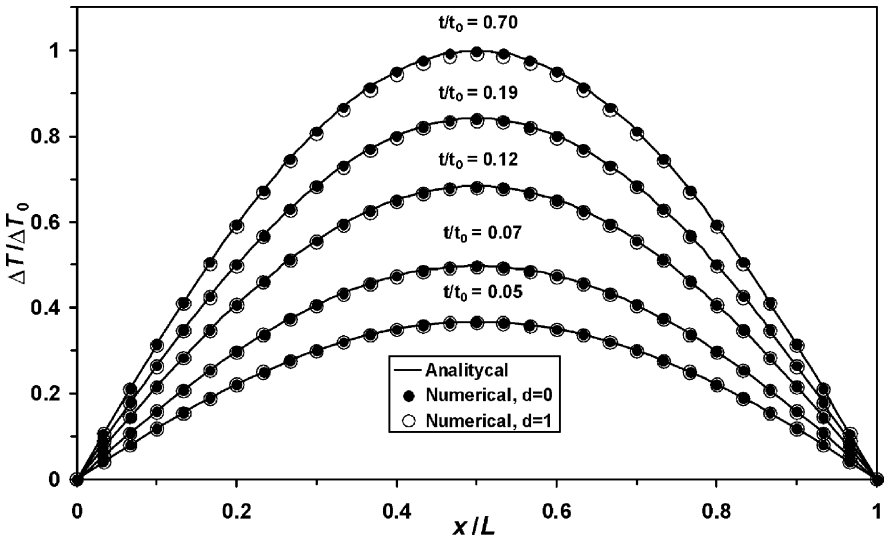

Fig. 7. The result of test of numerical solution for non-steady temperature changes within the Newtonian channel flow. Different symbols show the solutions calculated with ($d = 1$) and without ($d = 0$) numerical diffusion (see Eq. (12)). $t_0 = \rho C_p L^2/k$ is characteristic timescale, $\Delta T_0 = 5v_{z0}(\partial T_0/\partial z)\rho C_p L^2/(48k)$ is maximal temperature change in the center of the channel corresponding to the final steady temperature profile. Lateral resolution of the model: 31 nodes, 150 markers.

of gravity. Boundary conditions are taken as follows: zero vertical pressure gradient, $\partial P/\partial z = 0$ along the flow, $v_z = v_{z0}$, $T = T_0$ and $v_z = 0$, $\partial T/\partial x = 0$ at the walls. Viscosity of the flow is given by the following rheological equation (Turcotte and Schubert, 1982)

$$\eta = N \exp\left[1 - \frac{(T - T_0)}{T_0}\right] \exp\left[\frac{E}{RT_0}\right], \tag{20}$$

where E is the activation energy, R the gas constant and N the pre-exponential rheological constant, which

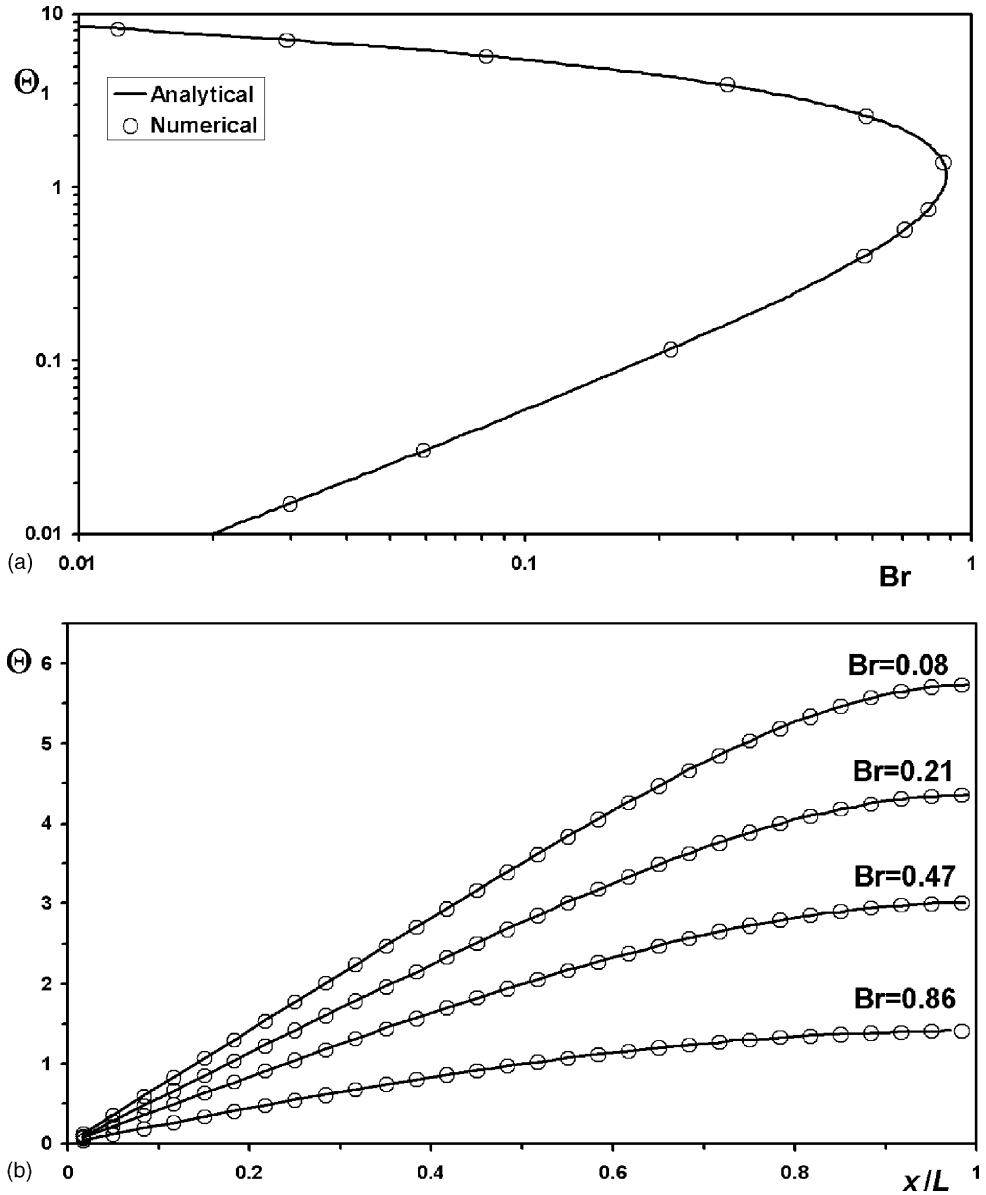

Fig. 8. Results of test of a numerical solution for the case of steady Couette flow with a temperature dependent viscosity (see Eq. (20)) and shear heating. $\Theta = E(T - T_0)/[R(T_0)^2]$ is non-dimensional temperature change; $\mathrm{Br} = (\sigma_{xz}L/T_0)^2 \times \exp(-E/RT_0)/(RkC_p)$ is Brinkman number. (a) Reproducing of analytical relations (Turcotte and Schubert, 1982) of maximal temperature change within the flow Θ_1 and Brinkman number Br and (b) comparison of analytical and numerical solutions for the distribution of temperature across the flow at different Brinkman number. Lateral resolution of the model: 32 nodes, 310 markers.

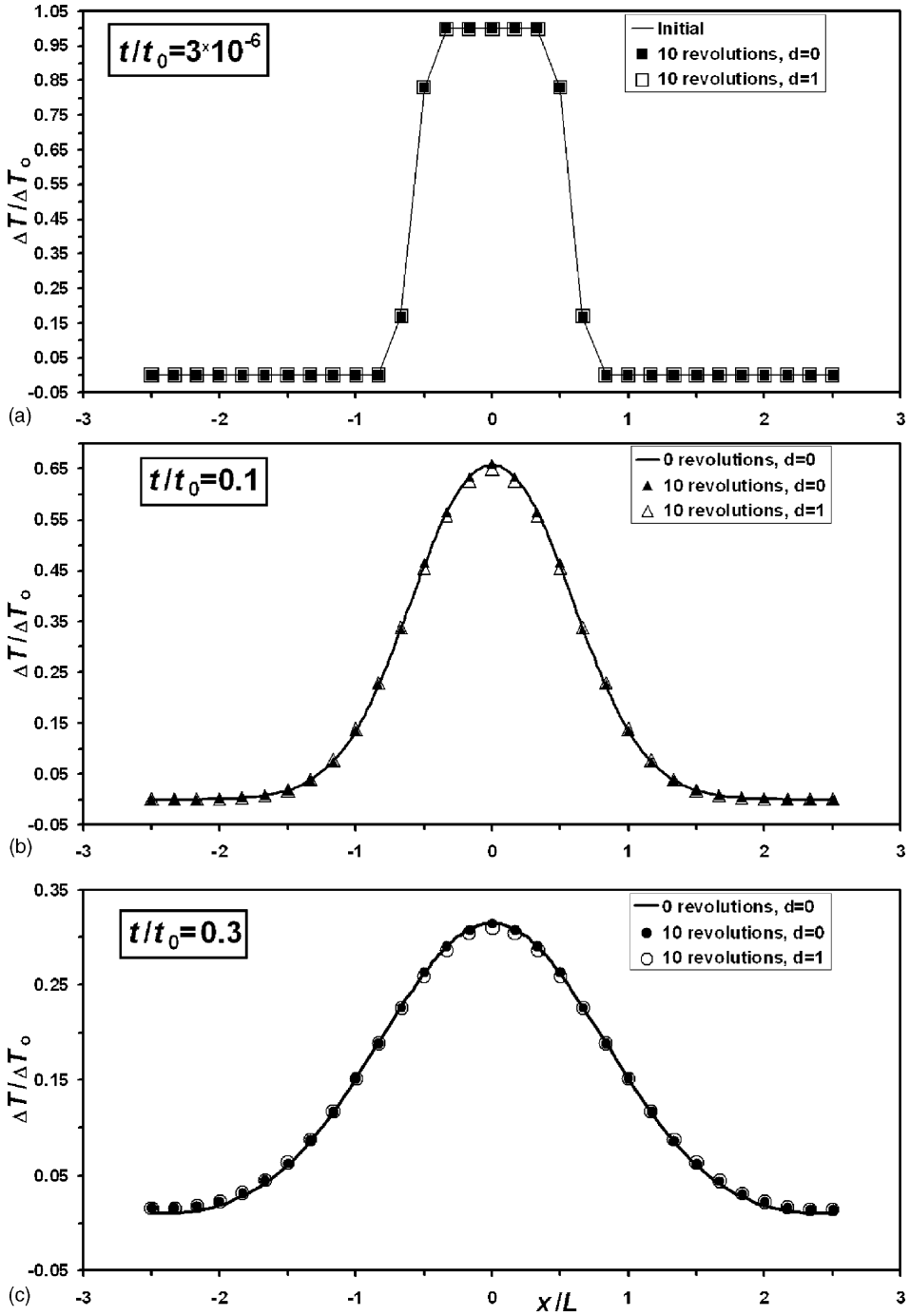

Fig. 9. The results of test of numerical solution for the solid body rotation of a square temperature wave. Figure shows the horizontal profiles across temperature wave at different time t after given number of revolutions. ΔT_0 and ΔT are initial and calculated amplitude of temperature waive, respectively; $t_0 = \rho C_p L^2/k$ is the characteristic timescale; d the numerical diffusion parameter (see Eq. (12)). Resolution of the model: 31×31 nodes, 150×150 markers.

depends on the material. Fig. 8 compares the results of numerical modeling of steady temperature profiles with analytical solution given by Turcotte and Schubert (1982). Both solutions merge together for a wide range of variations in the flow parameters, thus suggesting that adopted numerical technique allows us to solve accurately the coupled momentum and temperature equations in the case of temperature dependent rheology accompanied by significant shear heating.

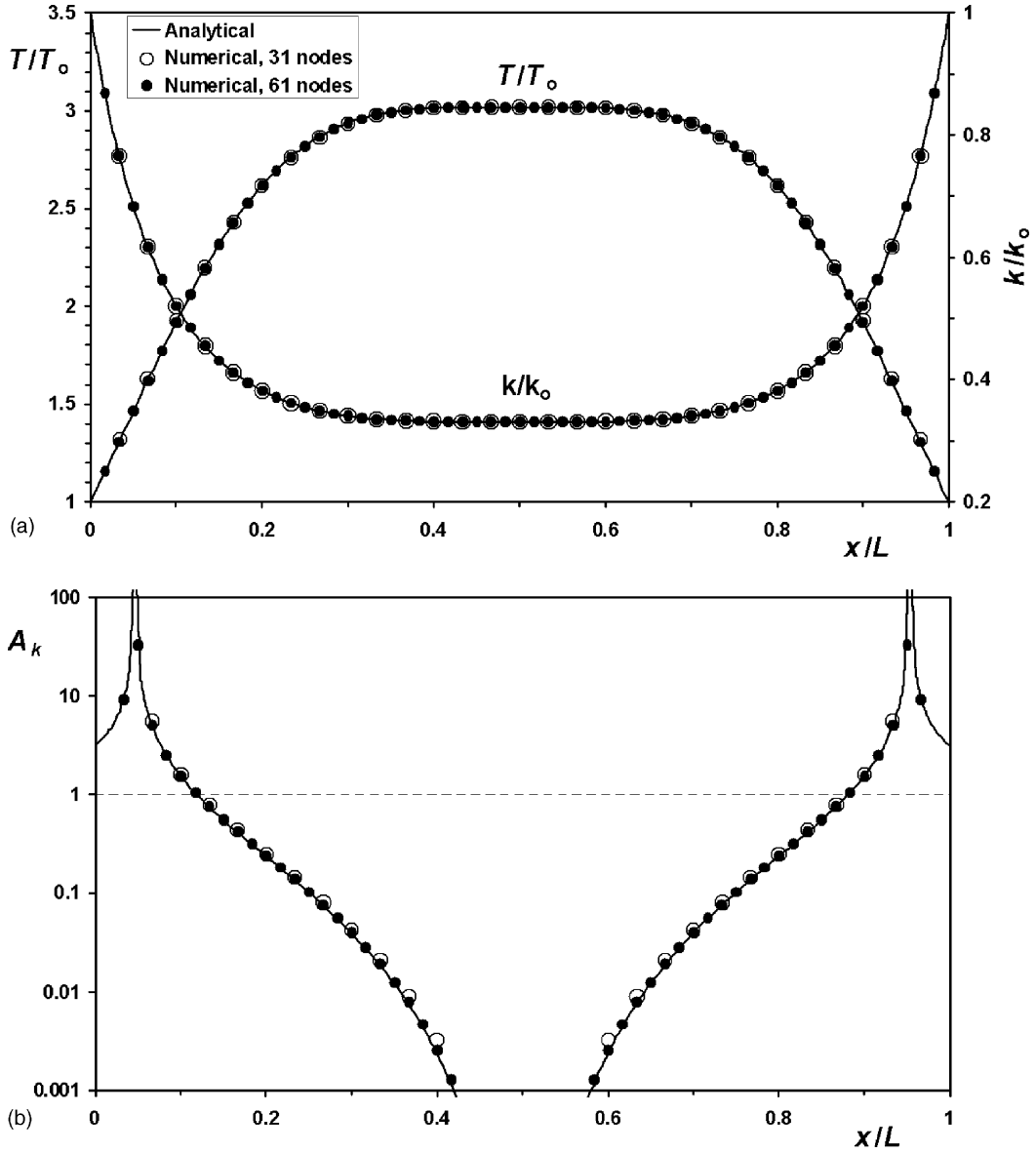

Fig. 10. Numerical solution for the case of steady channel flow with a temperature-dependent thermal conductivity described by Eq. (21). (a) Distribution of temperature T and thermal conductivity k and (b) distribution of parameter A_k characterizing temperature equation ($A_k = |[(\partial k/\partial T)(\nabla T)^2]/[k\,\Delta T]|$, see text for more details). T_0 is the temperature at the walls of the channel, k_0 the thermal conductivity at T_0. Different symbols show numerical results for different lateral resolution of the model (31 nodes/150 markers and 61 nodes/300 markers).

3.6. Advection of sharp temperature front

Verification of the ability to advect a temperature front is fundamental in many numerical tests (e.g., Malevsky and Yuen, 1991) and we have carried this out to check whether or not our scheme can meet this challenge of being capable to preserve a sharp front for a long time, as demonstrated in Malevsky and Yuen (1991) for the characteristics based method. In this connection we urge the reader to consult also the papers by Lenardic and Kaula (1993) and Smolarkiewicz and Margolin (1998) for the monotone treatment of the advective scheme. Numerical solutions are calculated for the solid body rotation of a two dimensional square temperature wave with widths L and an amplitude ΔT_0. The results of this test are shown in Fig. 9 for a moderate regularly spaced lateral grid resolution (31×31 nodes, 22,500 markers). In case of advection dominated heat transport (Fig. 9a) the adopted numerical advection scheme is obviously not diffusive, even for very many revolutions, as far as the initial positions of markers (with the corresponding values of initially prescribed temperature field been negligibly affected by the heat diffusion) are reproduced extremely well by the fourth-order Runge–Kutta integration scheme. In case of intermediate (Fig. 9b) and diffusion dominated (Fig. 9c) heat transport final temperature distribution does not depend notably on the number of revolutions. This point suggests a good conservation properties of adopted numerical scheme when advecting diffusing temperature fronts. Introducing of numerical diffusion (Eq. (12)) slightly affects temperature distribution in case of intermediate (Fig. 9b) and diffusion dominated (Fig. 9c) heat transport. Obviously, this numerical diffusion, which gives a small addition to the physical diffusion, exerts little influence in the case of advection dominated heat transport (Fig. 9a). Thus, our suggested characteristics based method of solving temperature equation using markers works very well in the different regimes of heat transport.

3.7. Channel flow with shear heating and variable thermal conductivity

We have conducted this test for verifying the accuracy of the code in flow situations where there are strong variations in temperature from shear heating and variable thermal conductivity for a moderate lateral grid resolution (31–61 nodes, 150–300 markers

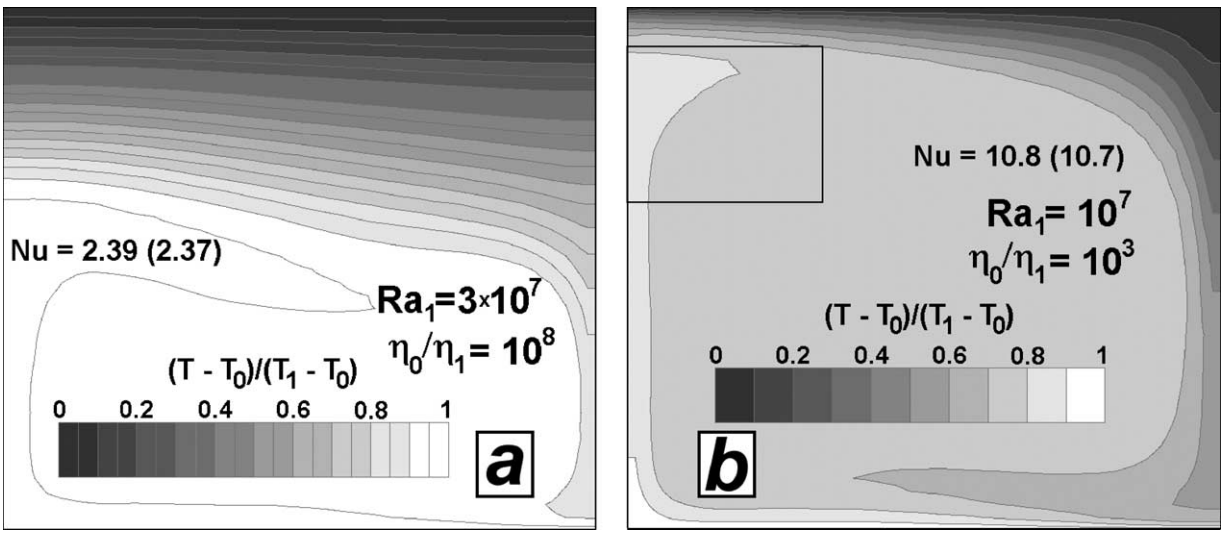

Fig. 11. Results of tests for stationary thermal convection in square box with temperature dependent viscosity (Eq. (25)) and constant thermal conductivity k. $Ra_1 = \alpha g \rho (T_1 - T_0)/(k\eta_1)$ is the Rayleigh number, $Nu = 1/L \int \partial T/\partial z \, dx$ is the calculated value of Nusselt number (in brackets are the values interpolated from Albers (2000) for given grid resolution). The effects of adiabatic and shear heat production are neglected. (a and b) Demonstrate numerical results for varying viscosity contrasts. Rectangle in (b) show area zoomed in Fig. 12. Model resolution: 43×43 nodes, 63504 markers.

across the channel). For this purpose we use vertical Newtonian channel flow (same as for test 4 but without temperature gradient along the channel) with a velocity distribution defined by Eq. (18) and shear heating, which provides a strong but linear heat-source term in the temperature equation, which is non-linear because of the temperature-dependent thermal conductivity. The thermal conductivity is taken to be decreasing with temperature, characteristic of phonons in crystal lattices (Hofmeister, 1999) according to the following relation (see also Schatz and Simmons, 1972)

$$k = \frac{k_0}{1 + b(T - T_0)/T_0}, \tag{21}$$

where T_0 is a constant temperature applied at the walls of the channel; k_0 the thermal conductivity at T_0; b the dimensionless coefficient.

Taking Eq. (18) for the velocity profile across the channel we calculate then shear heating term (H_s) for Eq. (4) and solve this equation analytically for steady case ($DT/Dt = 0$) using Eq. (21). The steady temperature profiles across the channel $T(x)$ are then defined by equation

$$T(x) = \frac{T_0[C(x) + (b-1)]}{b}, \tag{22}$$

$$C(x) = \exp\{L^4 b(1/2\partial P/\partial z)^2 \times [1 - (2x/L - 1)^4]/(48k_0T_0\eta)\},$$

where $\partial P/\partial z$ is the pressure gradient applied along the channel.

We define then dimensionless parameter A_k characterizing temperature equation in case of a strong temperature dependence of thermal conductivity as follows:

$$A_k = \left| \frac{(\partial k/\partial T)(\nabla T)^2}{k\,\Delta T} \right|. \tag{23}$$

When $A_k \ll 1$ the temperature Eq. (4) is parabolic and when $A_k \gg 1$ this equation become non-linear and hyperbolic-like (Barenblatt, 1996). In case of the aforementioned channel flow the formulation of A_k gives

$$A_k = \left| \frac{(\partial k/\partial T)(\partial T/\partial x)^2}{k(\partial^2 T/\partial x^2)} \right|. \tag{24}$$

Fig. 10 compares numerical and analytical results and shows strong (several orders of magnitude) variations (Fig. 10b) in parameter A_k in marginal zones of strong temperature gradient (Fig. 10a) resulted from significant shear heating. In this test a conductivity variation of a factor of 3 across the channel is obtained (Fig. 10a). The maximum value of A_k exceed 10^2 (actually, goes to infinity due to the change in the sign of $\partial^2 T/\partial x^2$) close to the walls where heat transport is mainly defined by the variations in thermal conductivity (Fig. 10a). Fig. 10 demonstrates the high accuracy of numerical solution, suggesting that adopted conservative FD scheme correctly treats the heat transport in case of strong variations in thermal conductivity.

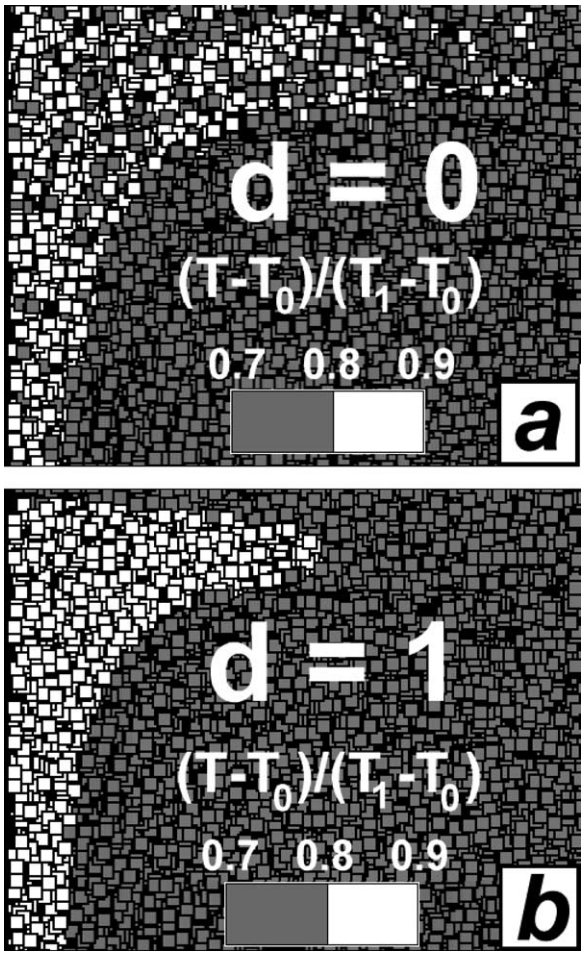

Fig. 12. Marker structure for zoomed-in area of the numerical model shown in Fig. 11b. Different colors of markers correspond to different value of temperature ascribed to the markers. (a and b) Show the results calculated without ($d = 0$) and with ($d = 1$) numerical diffusion (see Eq. (12)), respectively.

3.8. Thermal convection with a large viscosity contrast and constant thermal conductivity

Thermal convection with a large viscosity contrasts from temperature dependent viscosity is regarded as a challenging problem (Moresi and Solomatov, 1995). We have conducted tests to check the efficacy of our numerical scheme in coping ably with the temperature and momentum equations for convection with strong variations in temperature dependent viscosity. First, we study steady-state convection with a strong temperature-dependent viscosity in a square box of length L for a moderate irregularly-spaced lateral grid resolution (43 × 43 nodes, 63,504 markers). A factor of two compression in the FD grid has been applied to both the vertical and horizontal thermal boundary layers surrounding the box. The boundary conditions correspond to free-slip along all boundaries, a specified temperature on the top (T_0) and at the bottom (T_1) and $\partial T/\partial x = 0$ at the walls. Variable temperature-dependent viscosity, according to the Frank-Kamnetzky approximation (e.g., Moresi and Solomatov, 1995; Albers, 2000), is used

$$\eta = \eta_0 \exp\left[-\ln\left(\frac{\eta_0}{\eta_1}\right) \times \frac{T - T_0}{T_1 - T_0}\right], \tag{25}$$

where η_0 and η_1 are maximal and minimal values of viscosity, the defining given η_0/η_1. Benchmark results are shown in Fig. 11. Comparison (Fig. 11, values in brackets) of our results with those of Albers (2000) shows a good accuracy for large (10^3–10^8) viscosity contrast variations.

Fig. 12 compares the marker structure obtained without (Fig. 12a) and with (Fig. 12b) numerical

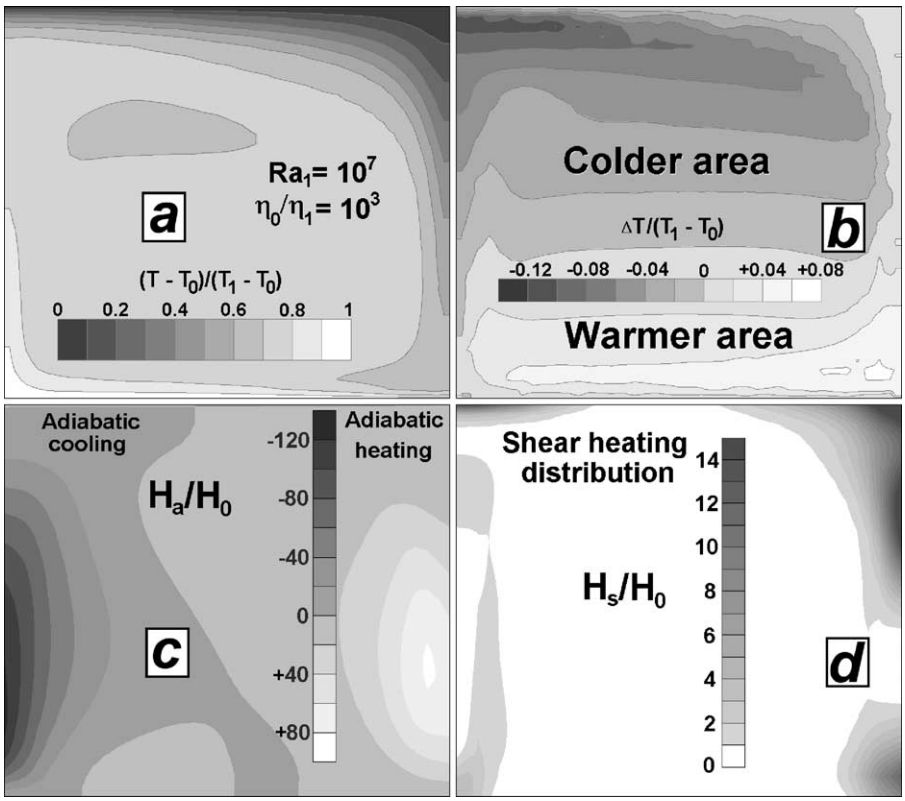

Fig. 13. Effects of shear and adiabatic heating on thermal convection. Model design and resolution correspond to Fig. 11b, box size—$L = 423$ km, pressure change from the top to the bottom of the model—$\Delta P = 12$ GPa, dissipation number—$D = 0.12$ ($D = \alpha g L/C_p$). (a) Temperature structure of the model; (b) temperature differences ΔT compared to the model neglecting shear and adiabatic heating (Fig. 11b); (c and d) thermal effects of adiabatic (H_a) and shear (H_s) heat production (see Eq. (4)), respectively. The value $H_0 = k(T_1 - T_0)/L^2$ is used for normalization.

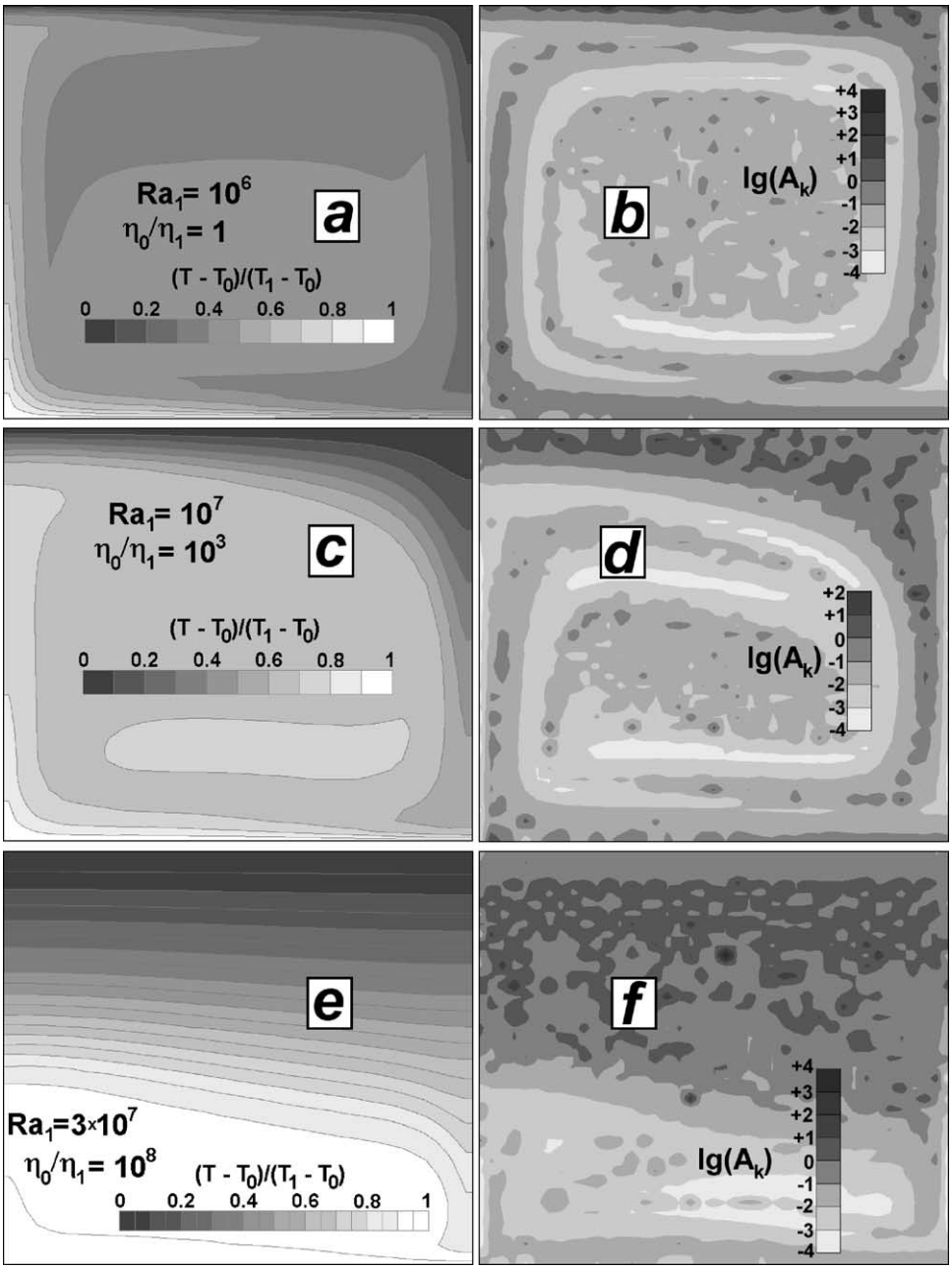

Fig. 14. Results of tests for stationary thermal convection in square box with temperature dependent viscosity (Eq. (25)) and thermal conductivity (Eq. (26)). Model design and resolution correspond to Fig. 13a. Rayleigh number is calculated as $Ra_1 = \alpha g \rho (T_1 - T_0)/(k_1 \eta_1)$, where k_1 and η_1 are, respectively, thermal conductivity and viscosity at bottom temperature T_1. All models include the effects of adiabatic and shear heating. *a*, *c* and *e*—thermal structure of the models. *b*, *d* and *f*—$A_k = |[(\partial k/\partial T)(\nabla T)^2]/[k\,\Delta T]|$ structure of the models. The patchy pattern of the A_k distribution corresponds to the Step 9 in Fig. 3 and is caused by the curvature of the Laplacian operator in the temperature field in the denominator of A_k and not by the gradient term in the numerator.

diffusion for the selected area of the model shown in Fig. 11b. Introducing the numerical diffusion with $d = 1$ (see Eq. (12)) removes unrealistic subgrid temperature oscillations present on markers (see Section 2.5) without affecting the accuracy of numerical solution of the temperature equation (see also Figs. 7 and 9).

The numerical simulations shown in Figs. 11 and 12 do not account for the effects of both shear and adiabatic heating to provide comparison with other authors who employed only the Boussinesq approximation (e.g., Albers, 2000; Moresi and Solomatov, 1995). However, these non-Boussinesq effects in the energetics can be very significant for modeling of mantle convection problems (Yuen et al., 2000a). Fig. 13a shows the temperature field resulting from the influence of adiabatic and shear heating on the thermal convection model shown in Fig. 11b for the same moderate regularly spaced lateral grid resolution (43 × 43 nodes, 63,504 markers). The changes in the temperature field at characteristic values of the box size ($L = 423$ km), pressure changes (0–12 GPa) and dissipation number ($D = 0.12$, where $D = \alpha g L / C_p$) are quite significant (8–12%, Fig. 13b). These changes are mainly resulted from adiabatic heating and cooling (Fig. 13c). The effects of shear heating appeared to be one-order of magnitude smaller (Fig. 13d).

3.9. Thermal convection with temperature dependent thermal conductivity and viscosity

These calculations are conducted to study 2D spatial distribution of parameter A_k (see Eq. (23)) characterizing the nature of the heat transport process in case of temperature dependent thermal conductivity for the moderate regularly spaced lateral grid resolution (43 × 43 nodes, 63,504 markers). This ratio measures the degree of non-linearity of heat transfer from variable thermal conductivity and indicates the local nature of the partial differential equation involving the temperature. The model setup is the same as in Section 3.8 and the variable thermal conductivity is defined by the following equation applicable for the ultramafic rocks of the upper Earth's mantle accounting for the phonon-dependence of the thermal conductivity (Hofmeister, 1999; Clauser and Huenges, 1995)

$$k = 0.73 + \frac{1293}{T + 77} \tag{26}$$

According to Eq. (26) the thermal conductivity contrast for studied upper mantle convection type models is $k_0/k_1 = 2.6$, where k_0 and k_1 are thermal conductivity in the top and at the bottom of the model, respectively. Shear and adiabatic heating effects are also taken into account in this extended-Boussinesq model. Fig. 14 demonstrate temperature and A_k structures of these models. Regions of high $A_k = 10^0$–10^2 values, which indicate a strong departure from the parabolic nature of the heat equation, are found in the upper portion of all studied models (Fig. 14b, d and f) characterizing zones of strong vertical gradients in temperature (Fig. 14a, c and e). Therefore, local changes in the parabolic character of temperature equation to a non-linear hyperbolic-like partial differential equation due to the variable thermal conductivity are relevant for the mantle convection models. Obviously, the correctness of numerical solution in the high A_k regions crucially depends on conservation nature of finite-difference formulation of the temperature equation. Another interesting feature of the A_k maps is the capture of the great details in the temperature advection pattern, which shows up much clearer than the temperature maps. This property can be exploited for visualization purposes for studying strongly time-dependent mantle convection with variable thermal conductivity.

4. Discussion and conclusions

In this paper, we have described a recently constructed numerical code, which is based on active or passive markers within the framework of a conservatively based finite-difference code (I2VIS) written in the C-language. There are several new features of this code worth emphasizing here. They include the following new capabilities with the following features:

1. The code can conserve stresses with strong variations of viscosity.
2. It can conserve heat-fluxes in time-dependent problems with sharply varying thermal conductivity, temperature gradients and shear heating.
3. It can conserve scalar fields, such as temperature field, density, chemical composition, and viscosity.
4. It can handle non-uniform FD grid with different stretching and compression factors.

These features are needed because of the increase in complexity in the physics of convection and other modeling problems in geothermal-mechanics. For example, we have delineated the regions in which the non-linear nature of the variable conductivity in heat-transfer problem is most obviously manifested (see Figs. 10 and 14). Previous codes can handle some of these non-linear aspects, but not all of them. For example, this is one of the first code to use markers as a variant of a characteristics based method (Malevsky and Yuen, 1991) for solving the temperature equation. De Smet et al. (1999) employed a variant of this characteristic method for compositional field in melting dynamics. We have also used the direct matrix inversion technique for solving both the momentum and temperature equations in 2D, thus obtaining more stable and higher accuracy solutions. This is made possible because of the increased memory now available on shared-memory parallel computer architecture. Solving directly a matrix associated with a 1000×1000 grid points, which amounts to around 100 Gbytes, is feasible on a single node of a shared-memory machine today. In the case of the temperature equation the implicit method allows for a much larger timestep than the commonly used explicit timestepping. Implicit methods are more desirable because of the non-linearities present in both the variable thermal conductivity and viscous heating terms, which are normally not included in many convection studies with the Boussinesq approximation (e.g., Solomatov and Moresi, 1997; Trompert and Hansen, 1996; Albers, 2000). We would like to stress the ease of the code implementation of the finite difference method combined with the marker techniques. This allows one to implement other routines, such as involving kinetics in phase transitions (Daessler and Yuen, 1996) or in grain-size dependent rheology (e.g., Kameyama et al., 1997), where ordinary differential equations for the kinetics are solved at each grid point. Our recent paper (Gerya and Yuen, 2003) provide an example of using developed numerical method for high resolution realistic modeling of topography, deformation, material/heat transport, shear/adiabatic heating, hydration and partial melting at subduction zones.

As future prospects for the method we envisage (i) parallelization of both marker-related calculations and direct matrix inversion using open MP paradigm for large shared-memory computers (Chandra et al., 2001), (ii) testing of very high resolution in 2D in term of both Eulerian (501×501 nodes) and Lagrangiqan (50 million markers) grids, (iii) adding viscoelastic rheology (e.g., Moresi et al., 2003) and (iv) introducing of an Eulerian grid allowing automated arbitrary resolution (e.g., Albers, 2001; Vasilyev et al., 1998).

The same marker technique can also be applied for advecting other scalar fields, such as composition and also vector and tensor quantities (e.g., Brackbill and Ruppel, 1986; Brackbill et al., 1988; Brackbill, 1991), which would have direct applications in thermal-chemical convection (Hansen and Yuen, 2000), the geodynamo (Glatzmaier, 2002) and viscoelastic stress-transfer (Melini et al., 2002; Moresi et al., 2003) problems. Similar approach using many tracers can be utilized for modeling high Deborah number compaction driven flows in poro-viscoelastic media (Vasilyev et al., 1998). By using a rotating Lagrangian frame of reference one can also solve efficiently the momentum equation in the dynamo problem with extremely large number markers in excess of 10^{10}, which are feasible in shared-memory architecture. This may help to resolve better the Ekman boundary layer (e.g., Desjardins et al., 2001). The work set out here lays the foundation for future in these aforementioned areas.

Acknowledgements

This work was supported by RFBR grant #03-05-64633, by an Alexander von Humboldt Foundation Research Fellowship to T.V. Gerya, and by the Sonderforschungsbereich 526 at Ruhr-University, funded by the Deutsche Forschungsgemeinschaft. Yuri Podladchikov and Shalva Amiranashvili are thanked for discussions and comments. Support of this research has come from the geophysics program of the National Science Foundation and the complex fluids program of the Department of Energy. Constructive reviews by two anonymous reviewers are greatly appreciated.

References

Albers, M., 2000. A local mesh refinement multigrid method for 3D convection problems with strongly variable viscosity. J. Comput. Phys. 160, 126–150.

Balmforth, N.G., Provenzale, A. (Eds.), 2001. Geomorphological Fluid Mechanics. Springer Verlag, Berlin, 578 pp.

Barenblatt, G.I., 1996. Scaling, Self-Similarity, and Intermediate Asymptotics, Cambridge University Press, Cambridge, 386 pp.

Batchelor, G.K., 1967. An Introduction to Fluid Dynamics. Cambridge University Press, New York, 615 pp.

Brackbill, J.U., 1991. FLIP MHD: a particle-in-cell method for magnetohydrodynamics. J. Comput. Phys. 96, 163–192.

Brackbill, J.U., Ruppel, H.M., 1986. FLIP: a method for adaptively zoned, particle-in-cell calculations of fluid flows in two dimensions. J. Comput. Phys. 65, 314–343.

Brackbill, J.U., Kothe, D.B., Ruppel, H.M., 1988. FLIP: a low dissipation, particle-in-cell method for fluid flow. Comput. Phys. Commun. 48, 25–38.

Chandra, R., Dagum, L., Kohr, D., Maydan, D., McDonald, J., Menon, R., 2001. Parallel Programming in OpenMP. Morgan Kaufmann, San Francisco, 230 pp.

Christensen, U.R., Yuen, D.A., 1984. The interaction of a subducting lithospheric slab with a chemical or phase boundary. J. Geophys. Res. 89, 4389–4402.

Christensen, U.R., Yuen, D.A., 1985. Layered convection induced by phase transitions. J. Geophys. Res. 90, 10291–10300.

Clauser, C., Huenges, E., 1995. Thermal conductivity of rocks and minerals. In: Ahrens, T.J. (Ed.), Rock Physics and Phase Relations. AGU Reference Shelf 3, AGU, Washington DC, pp. 105–126.

Daessler, R., Yuen, D.A., 1996. The metastable wedge in fast subducting slabs: constraints from thermokinetic coupling. Earth Planet. Sci. Lett. 137, 109–118.

Davies, J.H., Stevenson, D.J., 1992. Physical model of source region of subduction zone volcanics. J. Geophys. Res. 97, 2037–2070.

Desjardins, B., Dormy, E., Grenier, E., 2001. Instability of Ekman-Hartmann boundary layers, with application to the fluid flow near the core/mantle boundary. Phys. Earth Planet. Inter. 123, 15–26.

De Smet, J.H., van den Berg, A.P., Vlaar, N.J., Yuen, D.A., 2000. A characteristics-based method for solving the transport equation and its application to the process of mantle differentiation and continental root growth. Geophys. J. Int. 140, 651–659.

Dubuffet, F., Yuen, D.A., 2000. A thick pipe-like heat-transfer mechanism in the mantle: nonlinear coupling between 3D convection and variable thermal conductivity. Geophys. Res. Lett. 27, 17–20.

Dubuffet, F., Yuen, D.A., Yanagawa, T., 2000. Feedback effects of variable thermal conductivity on the cold downwellings in high Rayleigh number convection. Geophys. Res. Lett. 27, 2981–2984.

Dubuffet, F., Yuen, D.A., Rainey, E.S.G., 2002. Controlling thermal chaos in the mantle by positive feedback from radiative thermal conductivity. Nonlinear Proc. Geophys. 9, 311–323.

Fornberg, B., 1995. A Practical Guide to Pseudospectral Methods. Cambridge University Press, Cambridge, 231 pp.

Fountaine, F., Rabinowicz, M., Boulegue, J., 2001. Permeability changes due to mineral diagenesis in fractured crust: implications for hydrothermal circulation at mid ocean ridges. Earth Planet. Sci. Lett. 184, 407–425.

Gerya, T.V., Yuen, D.A., 2003. Rayleigh–Taylor instabilities from hydration and melting propel "cold Plumes" at subduction zones. Earth Planet. Sci. Lett. 212, 47–62.

Gerya, T.V., Perchuk, L.L., van Reenen, D.D., Smit, C.A., 2000. Two-dimensional numerical modeling of pressure–temperature–time paths for the exhumation of some granulite facies terrains in the Precambrian. J. Geodynam. 30, 17–35.

Gerya, T.V., Maresch, W.V., Willner, A.P., Van Reenen, D.D., Smit, C.A., 2001. Inherent gravitational instability of thickened continental crust with regionally developed low- to medium-pressure granulite facies metamorphism. Earth Planet. Sci. Lett. 190, 221–235.

Gerya, T.V., Perchuk, L.L., Maresch, W.V., Willner, A.P., Van Reenen, D.D., Smit, C.A., 2002. Thermal regime and gravitational instability of multi-layered continental crust: implications for the buoyant exhumation of high-grade metamorphic rocks. Eur. J. Miner. 14, 687–699.

Gerya, T.V., Yuen, D.A., Sevre, E.O.D., 2004. Dynamical causes for incipient magma chambers above slabs. Geology, in press.

Glatzmaier, G.A., 2002. Geodynamo simulations. How realistic are they? Annu. Rev. Earth Planet. Sci. 30, 237–257.

Hansen, U., Yuen, D.A., 2000. Extended-Boussinesq thermal-chemical convection with moving heat sources and variable viscosity. Earth Planet. Sci. Lett. 176, 401–411.

Hockney, R.W., Eastwood, J.W., 1981. Computer Simulations Using Particles, McGraw-Hill, New York.

Hofmeister, A.M., 1999. Mantle values of thermal conductivity and the geotherm from phonon lifetimes. Science 283, 1699–1706.

Kameyama, M., Kaneda, Y., 2002. Thermal-mechanical coupling in shear deformation of viscoelastic material as a model of frictional constitutive relations. Pure Appl. Geophys. 159, 2011–2028.

Kameyama, M., Yuen, D.A., Fujimoto, H., 1997. The interaction of viscous heating with grain-size dependent rheology in the formation of localized slip zones. Geophys. Res. Lett. 24, 2523–2526.

Kameyama, M., Yuen, D.A., Karato, S., 1999. Thermal-mechanical effects of low-temperature plasticity (the Peierls mechanism) on the deformation of a viscoelastic shear zone. Earth Planet. Sci. Lett. 168, 159–172.

Karato, S., 1997. Phase transformation and rheological properties of mantle minerals. In: Crossley, D., Soward, A.M. (Eds), Earth's Deep Interior. Gordon and Breach, New York, pp. 223–272.

Kincaid, C., Silver, P., 1996. The role of viscous dissipation in the orogenic process. Earth Planet. Sci. Lett. 142, 271–288.

Lenardic, A., Kaula, W.M., 1993. A numerical treatment of geodynamic viscous flow problems involving the advection of material interfaces. J. Geophys. Res. 98, 8243–8260.

Malevsky, A.V., Yuen, D.A., 1991. Characteristics-based methods applied to infinite Prandtl number thermal convection in the hard turbulent regime. Phys. Fluids A 3, 2105–2115.

Malevsky, A.V., Yuen, D.A., 1992. Strongly chaotic non-Newtonian mantle convection. Geophys. Astro. Fluid Dyn. 65, 149–171.

Melini, D., Cassarotti, E., Piersanti, A., Boschi, E., 2002. New insights on long distance fault interaction. Earth Planet. Sci. Lett. 204, 363–372.

Moresi, L.N., Solomatov, V.S., 1995. Numerical investigation of 2D convection with extremely large viscosity variations. Phys. Fluids 7, 2154–2162.

Moresi, L., Dufour, F., Mühlhaus, H.-B., 2003. A lagrangian integration point finite element method for large deformation modeling of viscoelastic geomaterials. J. Comput. Phys. 184, 476–497.

Oran, E.S., Boris, J.P., 1987. Numerical Simulation of Reactive Flow. Elsevier, New York, 601 pp.

Patankar, S.V., 1980. Numerical Heat Transfer and Fluid Flow, McGraw-Hill, New York.

Ramberg, H., 1981. Gravity, Deformation and Geological Application. Academic Press, London, 452 pp.

Ranalli, G., 1995. Rheology of the Earth, second ed. Chapman and Hall, London, 413 pp.

Regenauer-Lieb, K., Yuen, D.A., Branlund, J., 2001. The initiation of subduction: critically by addition of water? Science 294, 578–580.

Richard, G., Monnereau, M., Ingrin, J., 2002. Is the transition zone an empty water reservoir? Inferences from numerical model of mantle dynamics. Earth Planet. Sci. Lett. 205, 37–51.

Riedel, M.R., Karato, S., 1997. Grain-size evolution in subducted oceanic lithosphere associated with the olivine-spinel transformation and its effects on rheology. Earth Planet. Sci. Lett. 148, 27–43.

Schatz, J.F., Simmons, G., 1972. Thermal conductivity of earth materials at high temperatures. J. Geophys. Res. 77, 6966–6983.

Schott, B., Schmeling, H., 1998. Delamination and detachment of a lithospheric root. Tectonophysics 296, 225–247.

Smolarkiewicz, P.K., Margolin, L.G., 1998. MPDATA: a finite-difference solver for geophysical flows. J. Comput. Phys. 140, 459–480.

Solomatov, V.S., Moresi, L.-N., 1997. Three regimes of mantle convection with non-Newtonian viscosity and stagnant lid convection on the terrestrial planets. Geophys. Res. Lett. 24, 1907–1910.

Tackley, P.J., 1996. Effects of strongly variable viscosity on three-dimensional compressible convection in planetary mantles. J. Geophys. Res. 101, 3311–3332.

Ten, A.A., Yuen, D.A., Podladchikov, Yu.Yu., 1999. Visualization and analysis of mixing dynamical properties in convecting systems with different rheologies, Electron. Geosci. 4.

Tikhonov, A.N., Samarsky, A.A., 1972. Equations of Math Physics. Nauka, Moscow (in Russian).

Trompert, R.A., Hansen, U., 1996. The application of a finite-volume multigrid method to three-dimensional flow problems in a highly viscous fluid with variable viscosity. Geophys. Astrophys. Fluid Dyn. 83, 261–291.

Van den Berg, A.P., Yuen, D.A., Steinbach, V., 2001. The effects of variable thermal conductivity on mantle heat transfer. Geophys. Res. Lett. 28, 575–578.

Vasilyev, O.V., Podladchikov, Y.Y., Yuen, D.A., 1998. Modeling of compaction driven flow in poro-viscoelastic medium using adaptive wavelet collocation method. Geophys. Res. Lett. 25, 3239–3243.

Virieux, J., 1986. P-SV wave propagation in heterogeneous media: velocity–stress finite-difference method. Geophys. 51, 889–901.

Weinberg, R.B., Schmeling, H., 1992. Polydiapirs: multiwavelength gravity structures. J. Struct. Geol. 14, 425–436.

Wesseling, P., 1992. An Introduction to Multigrid Methods. Wiley, New York, 1992.

Woods, A.W., 1999. Liquid and vapor flow in superheated rock. Annu. Rev. Fluid Mech. 31, 171–200.

Yuen, D.A., Balachandar, S., Hansen, U., 2000a. Modeling mantle convection: a significant challenge in geophysical fluid dynamics. In: Fox, P.A., Kerr, R.M. (Eds.), Geophysical and Astrophysical Convection. Gordon and Breach, London, pp. 257–293.

Yuen, D.A., Vincent, A.P., Bergeron, S.Y., Dubuffet, F., Ten, A.A., Steinbach, V.C., Starin, L., 2000b. Crossing of scales and non-linearities in geophysical processes. In: Boschi, E., Ekstrom, G., Morelli, A. (Eds.), Problems for the New Millennium. Editrice Compositori, Bologna, Italy, pp. 403–463.